Journal of Asian Earth Sciences 239 (2022) 105417

Contents lists available at ScienceDirect

Journal of Asian Earth Sciences

journal homepage: www.elsevier.com/locate/jseaes

Organic matter enrichment due to high primary productivity in the deep-water shelf: Insights from the lower Cambrian Qiongzhusi shales of the central Sichuan Basin, SW China

Qiang Li [a,b], Guangdi Liu [a,b,*], Zezhang Song [a,b,*], Benjian Zhang [c], Mingliang Sun [a,b], Xingwang Tian [c], Dailin Yang [c], Yunlong Wang [c], Lianqiang Zhu [a,b], Yushun Cao [a,b]

[a] State Key Laboratory of Petroleum Resources and Prospecting, China University of Petroleum, Beijing 102249, China
[b] College of Geosciences, China University of Petroleum, Beijing 102249, China
[c] Exploration and Development Research Institute of Southwest Oil & Gas Field Company, PetroChina, Chengdu 610041, China

ARTICLE INFO

Keywords:
Primary productivity
Shales
Hydrothermal activity
Cambrian
Deep-water shelf
Sichuan Basin

ABSTRACT

The formation and enrichment mechanisms of organic-rich shales under different marine environments remain unclear. Recently, Cambrian Qiongzhusi (QZS) shales with greater thickness and total organic carbon (TOC) content were found in a deep-water shelf (DWS) than in the adjacent shallow-water shelf (SWS) of the central Sichuan Basin, and these locations provide ideal conditions for determining the mechanisms underlying differences in organic matter (OM) enrichment. In this study, we investigated the TOC, pyrolysis, organic carbon isotopes ($\delta^{13}C_{org}$), biomarkers, and elemental geochemistry of the QZS shales. Based on a detailed comparison between shales from the DWS to the SWS, an OM enrichment model of different shelf conditions was established and the reasons for the higher TOC content in the DWS were clarified. The deposition of QZS shales was accompanied by a large-scale regional transgression. Against the background of an overall humid climate, the water mass at the bottom of the DWS was more restricted, resulting in limited external material exchange and supply. The water mass of the DWS represented by the bottom of the QZS was anoxic and showed the development of euxinic conditions. The biogenic Ba (Ba_{bio}) content of the samples in the DWS under deep basinal conditions was significantly greater than that in the SWS region, which reflects higher primary productivity and is associated with a large accommodating space and upwelling flows caused by the hydrothermal activities in the DWS. Under conditions in which OM enrichment is dominated by productivity, the DWS is a more favorable location for the formation of high-quality shales.

1. Introduction

Organic-rich shales can serve as the material basis for hydrocarbon generation in sedimentary basins and represent an essential target for unconventional shale oil and gas exploration (Zou et al., 2019). Therefore, studying the formation mechanism of these shale sediments, particularly the deep and ancient shales of the Cambrian System, is of great significance. The formation of organic-rich shales in associated with the gradual enrichment of the initial organic matter (OM), and this process controls the content and distribution characteristics of OM. Previous studies have shown that OM enrichment is affected by factors such as primary productivity (Dymond et al., 1992; Müller and Suess, 1979; Pedersen and Calvert, 1990; Tribovillard et al., 2006), waterbody redox environment (Canfield, 1989; Demaison and Moore, 1980), climatic conditions (Leythaeuser, 1973; Roy and Roser, 2013), sedimentation rate (Canfield, 1994; Ibach, 1982; Murphy et al., 2000; Sageman et al., 2003), and other abnormal events (Shen et al., 2013). Several geochemical proxies have been established to determine how various factors affect OM enrichment, including total organic carbon (TOC), biogenic Ba (Ba_{bio}), strontium to barium ratio (Sr/Ba), uranium enrichment factor (U-EF), molybdenum to TOC ratio (Mo/TOC), and titanium to aluminum ratio (Ti/Al) (Algeo and Liu, 2020; Murphy et al., 2000; Schoepfer et al., 2015; Tribovillard et al., 2012).

Fine-grained sediments of the same layer may have different sedimentary conditions not only in the longitudinal direction but also in the planar direction (Williams et al., 2022; Wu et al., 2020). Previous studies

* Corresponding authors at: State Key Laboratory of Petroleum Resources and Prospecting, China University of Petroleum, Beijing 102249, China.
E-mail addresses: lgd@cup.edu.cn (G. Liu), songzz@cup.edu.cn (Z. Song).

https://doi.org/10.1016/j.jseaes.2022.105417
Received 15 April 2022; Received in revised form 15 September 2022; Accepted 19 September 2022
Available online 24 September 2022

have revealed differences between the organic carbon isotope ($\delta^{13}C_{org}$) values of the deep-water shelf (DWS) and shallow-water shelf (SWS) and showed that the $\delta^{13}C_{org}$ values of the DWS shales are lower than those of the SWS shales (Fang et al., 2019; Jiang et al., 2007). However, most studies have focused on the redox conditions and inorganic–organic carbon pool cycling in the water mass under different shelf conditions (Guo et al., 2007; Jiang et al., 2007; Mcfadden et al., 2008; Song et al., 2021; Yang et al., 2022), whereas less attention has been focused on differential OM enrichment.

The Ediacaran–Cambrian is an important period in the evolution of the global environment, marine systems, and ecosystems (Guo et al., 2007; Hoffman et al., 1998; Kimura and Watanabe, 2001; Walter et al., 2000). An extensive anoxic deposition and negative $\delta^{13}C_{org}$ anomaly was formed at the boundary between the Precambrian and Cambrian (PC–C) (Jacobsen and Kaufman, 1999; Kimura and Watanabe, 2001; Xiao et al., 2017; Xiao et al., 2021), with special Sr, S, and Si isotopic responses (Condon et al., 2005; Knoll et al., 1986; Veizer et al., 1997). During the PC–C period, under a background of large-scale

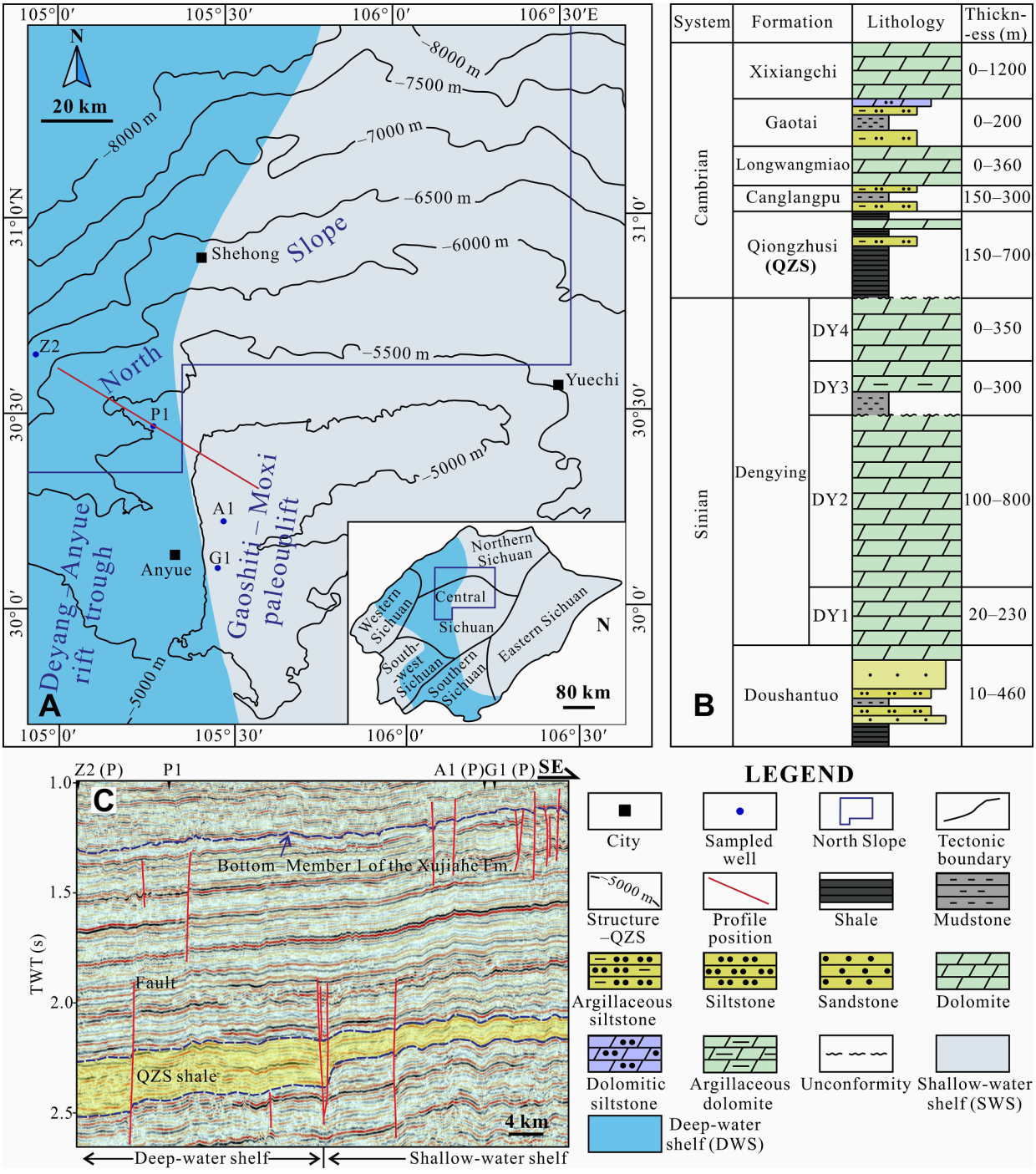

Fig. 1. (A) Tectonic units (Xu et al., 2020), paleogeography during the Ediacaran-Cambrian transition (Fan et al., 2021; Li et al., 2022; Yang et al., 2021), and sampling wells of the central Sichuan Basin. (B) Stratigraphic column illustrating the Ediacaran and Cambrian System. Modified from Zhu et al. (2015). (C) Seismic profile crossing the deep-water shelf (DWS) and shallow-water shelf (SWS). The location of the seismic profile is shown in Fig. 1A. The yellow highlighted area indicates the horizontal distribution of the Cambrian Qiongzhusi Formation (QZS), and (P) represents the projection position. (For interpretation of the references to colour in this figure legend, the reader is referred to the web version of this article.)

transgression, the Lower Cambrian Qiongzhusi Formation (QZS) shales were extensively distributed on the Upper Yangtze Platform of South China (Guo et al., 2007; Yeasmin et al., 2017). Almost all Sinian and Cambrian gas reservoirs in the Sichuan Basin are sourced from this set of shales, including the giant Weiyuan and Anyue gas fields (Gao et al., 2017; Shi et al., 2018, 2020; Zou et al., 2014). Previous research has mainly focused on the QZS shales in the Gaoshiti – Moxi paleouplift (SWS), including the evolution of the sedimentary environment (Gao et al., 2016, 2021; Wang et al., 2020), generation of hydrocarbons (Qiu et al., 2021), and origin of the OM (Wang et al., 2019; 2021). These investigations showed that compared with other fine-grained sediments of the Sinian–Cambrian System in the Sichuan Basin, the QZS shales are characterized by a high TOC content and negative $\delta^{13}C_{org}$ values and they present a higher anoxic degree, higher TOC content (avg. 1.87 %), and lower $\delta^{13}C_{org}$ values (avg. –32.91 ‰) in the bottom section (Wang et al., 2015) but a typical dysoxic – oxic environment in the top section (Gao et al., 2016; Wang et al., 2020).

In sharp contrast, QZS shales that developed in the DWS have not received much attention because of their lower exploration degree and greater burial depth. In 2020, two new wells (P1 and Z2) in the North Slope area made a significant breakthrough in gas exploration (1.219×10^6 m^3/d in well P1; Zhao et al., 2020b). Data based on exploration well samples revealed that the shales in the DWS have a higher TOC content than those in the SWS; however, the mechanism underlying differential OM enrichment was not clarified.

In this study, we performed mineralogical, organic, and elemental geochemical analyses based on the latest core data collected from the North Slope area. Based on this series of geochemical analyses, the objectives of this study were to (1) reconstruct the water mass sedimentary conditions of the QZS shales in the DWS and (2) clarify the enrichment mechanism of organic-rich black shales in the SWS and DWS regions to expand the theoretical research on OM enrichment under different marine environments.

2. Geological setting

The Sichuan Basin has an area of approximately 18×10^4 km^2, with six first-ordered tectonic units (Fig. 1A). The central Sichuan flat-gentle structural area is situated at the center of the Sichuan Basin (Wei et al., 2014), and the basement of the basin is composed of pre-Sinian magmatic and metamorphic rocks. The basin was transformed into a foreland basin (Late Triassic-Quaternary) after the craton developed (Ediacaran-Middle Triassic), and it has an overall sedimentary thickness of approximately 8000–12000 m. Vertically, the Doushantuo and Dengying Formations (DY) are in the Sinian System (Fig. 1B). The Doushantuo Formation is dominated by sand shale interbeds, the DY1 is primarily composed of argillaceous and silty dolomite, and the DY2 is dominated by algal dolomite intercalated with silty dolomite, micritic dolomite, and granular dolomite, while the karst cavity at the top of the DY2 resulted from Tongwan-I movement (Xu et al., 2012). A set of shales is deposited at the bottom of the DY3, whereas fine-grained silty layered dolomite dominates the top (Wei et al., 2017), and silt dolomite, granular clastic dolomite, dissolved pore silt dolomite, and algal dolomite are deposited in the DY4. Owing to the Tongwan-II movement, an unconformity occurs between the Cambrian System and Dengying Formation, with an erosion thickness of approximately 50–200 m (Xu et al., 2012). The Cambrian System is vertically divided into the QZS, Canglangpu, Longwangmiao, Gaotai, and Xixiangchi Formations (Fig. 1B). The QZS is dominated by shale with a small amount of argillaceous siltstone and is also the largest source rock in the central Sichuan Basin, especially in the Deyang–Anyue rift trough and North Slope area (Fig. 1C). During the Cambrian depositional period, the Sichuan Basin was carbonate platform facies, of which the Deyang-Anyue rift trough and part of the North Slope area were DWS facies and the rest were SWS facies (Fig. 1A).

The North Slope is located to the north of the Gaoshiti–Moxi paleouplift (Fig. 1A). At present, the North Slope has a wide monoclinic structure, with a maximum depth of the DY4 reaching –8300 m. The dip angle of the stratum on the north side of the uplift increased from the late Indosinian to the early Yanshanian and was finalized (Ma et al., 2020). The DY2 on the North Slope of the Sichuan Basin represents a new field for natural gas exploration, with natural gas found in wells P1 and Z2, and it has an average reservoir porosity of 3.5 %. All discovered gas reservoirs were lithologic traps that were sealed by the overlying shale and lateral micritic dolomite (Xu et al., 2020; Zhao et al., 2020b).

3. Samples and analytical methods

3.1. Samples

Thirty-three shale samples in this study were obtained from the cores of two wells in the DWS (Fig. 1A). Some samples were selected for thin section analysis and scanning electron microscopy (SEM). After removing the impurities, all samples were ground to 200 mesh using an agate mortar for Rock-Eval pyrolysis and TOC and $\delta^{13}C_{org}$ analyses. Twelve samples were selected for X-ray diffraction (XRD) and major element, trace element (TE), and rare earth element (REE) analyses. Three samples were selected for gas chromatography–mass spectrometry (GC–MS) analysis.

3.2. Analytical methods

The TOC test was performed using a LecoCS-200 carbon/sulfur analyzer after removing the carbonate with dilute hydrochloric acid ($HCl:H_2O = 1:7$) (Espitalie et al., 1977). Rock pyrolysis was performed using a Rock-Eval II instrument (Peters, 1986), and parameters such as the free and volatile hydrocarbons (S_1) and remaining hydrocarbon generative potential (S_2) were obtained. The $\delta^{13}C_{org}$ analysis was performed using a Finnigan MAT 253 isotope ratio mass spectrometer. The test results are in per thousand (‰), relative to the Vienna Pee Dee Belemnite (VPDB) standard value, and they are presented in Table 1. Thin sections were observed under a Leica DM4500P microscope. The above analysis was conducted at the State Key Laboratory of Petroleum Resources and Prospecting at the China University of Petroleum, Beijing (CUPB).

The SEM samples were obtained from fresh sections with gold on the surface, which enhanced the electrical conductivity. A Quanta-200F field emission scanning electron microscope with an energy dispersive X-ray spectrometer was used to precisely measure the elemental composition. This analysis was performed at the Microstructure Laboratory for Energy Materials, CUPB. XRD was performed at the State Key Laboratory of Heavy Oil Processing, CUPB.

The major element, TE, and REE were measured using an ELEMENT XR plasma mass spectrometer. X-ray fluorescence spectroscopy was employed to measure the oxides of major elements, and inductively coupled-plasma mass spectrometry (ICP-MS) was used to measure the TE and REE. First, 0.050 g of the sample was accurately weighed into a polytetrafluoroethylene bomb, and HNO_3 and HF were added and maintained at 185 °C for 24 h to dissolve the samples. The remaining solution was then heated to evaporation at 160 °C, and HNO_3 was added again to melt the material, which was then diluted with dilute HNO_3 to generate a 50 mL solution. This solution was directly tested using ICP-MS, and the relative standard deviation of the standard samples was<5 %. Detailed test procedures for element B were reported by Remírez and Algeo (2020). This analysis was performed at the Analytical Laboratory of the Beijing Research Institute of Uranium Geology. The results are presented in Tables 2 and 3.

Soxhlet extraction was performed for 72 h, and the extractable organics were separated into saturated hydrocarbons, aromatic hydrocarbons, nonhydrocarbons, and asphaltenes as described in detail by Wang et al. (2019). GC–MS analysis of the saturated fraction was conducted using an Agilent 7890-5975C instrument, with an HP-5MS elastic silica capillary column (60 mm × 0.25 mm × 0.25 μm). Based on the

Table 1
General geochemical features and carbon isotopes of shales in the Cambrian Qiongzhusi Formation of the deep-water shelf, central Sichuan Basin.

Sample	Depth	TOC	S_1	S_2	$S_1 + S_2$	$\delta^{13}C_{org}$
	(m)	(%)	(mg/g)	(mg/g)	(mg/g)	(‰)
Z2–1[a]	5911.09	2.24	1.70	0.39	2.09	–34.6
Z2–2	5911.36	2.24	1.53	0.31	1.84	–34.4
Z2–3[a]	5912.46	2.94	3.70	0.53	4.23	–34.5
Z2–4	5913.46	2.50	1.70	0.34	2.04	–34.6
Z2–5	5916.97	1.61	1.32	0.26	1.58	–34.3
Z2–6[a]	5917.06	1.64	1.95	0.31	2.26	–33.9
Z2–7	6318.68	0.28	0.08	0.04	0.12	–32.9
Z2–8	6318.78	3.13	1.24	0.41	1.65	–35.3
Z2–9	6319.54	9.81	0.01	0.08	0.09	–36.4
Z2–10[a]	6324.54	2.46	1.19	0.32	1.51	–34.6
Z2–11	6327.75	2.49	0.90	0.32	1.22	–34.4
Z2–12	6327.80	0.54	0.43	0.10	0.53	–33.3
Z2–13[a]	6327.86	2.03	1.67	0.38	2.05	–33.9
Z2–14[a,b]	6328.94	3.65	0.79	0.39	1.18	–35.2
P1–1[a]	5305.74	3.50	0.03	0.15	0.18	N–D
P1–2[a]	5305.94	1.67	0.03	0.04	0.07	–34.0
P1–3[b]	5307.34	1.57	0.02	0.02	0.04	–33.4
P1–4	5307.62	1.68	0.02	0.02	0.04	–33.4
P1–5	5583.00	1.36	0.01	0.04	0.05	–35.9
P1–6	5583.99	1.30	0.02	0.03	0.05	–36.8
P1–7	5584.10	1.27	0.01	0.03	0.04	–36.5
P1–8[a]	5585.15	5.23	0.01	0.08	0.09	–34.8
P1–9[a]	5585.28	2.72	1.54	0.46	2.00	–34.6
P1–10	5585.57	1.75	0.02	0.05	0.07	–36.0
P1–11	5586.52	2.04	0.01	0.03	0.04	–36.3
P1–12	5586.60	2.12	0.01	0.02	0.03	–36.9
P1–13	5587.45	2.28	0.01	0.02	0.03	–37.1
P1–14	5588.56	2.13	0.01	0.02	0.03	–35.5
P1–15[a,b]	5589.48	1.57	0.02	0.05	0.07	–35.5
P1–16	5589.49	0.78	0.01	0.03	0.04	–34.7
P1–17[a]	5590.50	2.00	0.03	0.05	0.08	–35.9
P1–18	5591.23	1.01	0.01	0.06	0.07	–35.6
P1–19	5591.41	1.49	0.01	0.05	0.06	–35.4

Note: [a] samples with major, trace, and rare earth elements. [b] samples with GC–MS. N–D, not determined.

peak areas in the *m/z* 217 fragmentograms, the relative abundances of steranes were finally obtained. This analysis was performed at the State Key Laboratory of Heavy Oil Processing, CUPB.

4. Results

4.1. Mineralogical and petrological characteristics

The QZS shales exhibit fine grains with a maximum grain size of approximately 100 μm (Fig. 2A). Under the microscope, quartz, pyrite, and OM were widely distributed, among which quartz was the most abundant (Fig. 2A–D). OM was present in a banded or macroscopic form (Fig. 2D–F, H). Moreover, the mineral composition included feldspar (Fig. 2G, I) and dolomite (Fig. 2J, L). The XRD results indicated that the quartz content was highest (avg. 37.8 %). The carbonate minerals were mainly dolomite (avg. 14.96 %), and some samples had high calcite contents (53.3 %, P1–8). One sample contained no clay minerals, although the remaining samples had an average clay content of 24.1 %. The average pyrite content was 5.28 %, and K-feldspar and plagioclase were also present (Fig. 3). The mineral characteristics were similar to those reported in a study of the QZS shales in the Gaoshiti–Moxi paleouplift (SWS) by Gao et al. (2016), which provides a basic framework for research on differences in OM enrichment under different marine environments.

4.2. Organic geochemistry

The average TOC content in the DWS (2.27 %, n = 33) was considerably higher than that in the SWS (avg. 1.87 %, n = 79) (Fig. 4). The TOC values of well P1 ranged from 0.78 % to 5.23 % (avg. 1.97 %, n = 19). The values of 18 samples were>1.0 %, seven of which were>2.0 % (Table 1). The TOC values of well Z2 varied between 0.28 % and 9.81 % (avg. 2.68 %, n = 14). Twelve samples had values>1.0 %, 10 of which had values>2.0 %. Due to the high maturity, the S_1 and S_2 values were extremely low (Hossain et al., 2009), with ranges of 0.01–3.70 mg/g (avg. 0.61 mg/g, n = 33) and 0.02–0.53 mg/g (avg. 0.16 mg/g, n = 33), respectively. The $\delta^{13}C_{org}$ values ranged from –37.1 ‰ to –33.4 ‰ (avg. –35.46 ‰, n = 18) for well P1 and –36.4 ‰ to –32.9 ‰ (avg. –34.45 ‰,

Table 2
Major element concentrations of shales in the Cambrian Qiongzhusi Formation of the deep-water shelf and shallow-water shelf, central Sichuan Basin.

Sample	Depth	SiO_2	Al_2O_3	Fe_2O_3	MgO	CaO	Na_2O	K_2O	MnO	TiO_2	P_2O_5
	(m)	(%)									
Z2–1	5911.09	63.16	11.31	4.54	2.68	2.93	2.03	3.44	0.06	0.63	0.327
Z2–3	5912.46	62.91	11.51	4.88	2.5	2.56	2.11	3.68	0.054	0.532	0.394
Z2–6	5917.06	66.08	11.85	3.41	2.36	2.47	2.31	3.31	0.057	0.71	0.306
Z2–10	6324.54	68.32	10.06	4.03	1.96	3.08	1.68	2.42	0.057	0.577	0.185
Z2–13	6327.86	64.1	11.83	5.41	2.33	2.56	1.95	2.87	0.053	0.68	0.177
Z2–14	6328.94	61.58	11.22	4.7	2.18	4.93	1.97	2.45	0.061	0.556	0.181
P1–1	5305.74	65.03	13.93	5.18	2.15	1.45	2.12	2.92	0.039	1.01	0.227
P1–2	5305.94	66.13	12.01	4.1	1.97	1.54	2.34	2.81	0.038	0.687	0.227
P1–8	5585.15	7.74	0.553	0.449	1.91	49.04	0.235	0.107	0.31	0.038	9.9
P1–9	5585.28	72.89	8.61	3.3	1.61	2.15	1.55	2.14	0.055	0.466	0.167
P1–15	5589.48	28.86	1.1	0.585	9.08	27.62	0.043	0.602	0.789	0.055	9.71
P1–17	5590.5	66.74	0.334	0.318	2.26	14.9	0.042	0.116	0.094	0.021	7.5
A1–1*	5028.67	64.39	11	3.3	2.99	3.76	1.52	3.21	0.049	0.671	0.234
A1–2*	5032.63	67.76	11.79	3.04	2.11	2.02	1	3.9	0.023	0.775	0.267
A1–3*	5034.27	64.4	13.21	4.04	2.44	1.95	0.332	4.71	0.025	0.76	0.255
G1–1*	4895.99	63.29	14.97	4.43	1.83	1.52	1.21	4.15	0.024	0.829	0.649
G1–2*	4980.87	64.87	12.99	5.11	1.89	1.62	1.58	3.42	0.027	0.734	0.239
G1–3*	4981.25	62.96	12.91	3.54	2.96	3.2	1.47	3.46	0.055	0.767	0.236
G1–4*	4981.37	63.2	13.76	4.8	2.22	1.98	1.49	3.64	0.031	0.801	0.243
G1–5*	4983.23	61.73	13.54	4.35	2.95	2.99	1.36	3.73	0.039	0.782	0.235
G1–6*	4983.91	62.54	11.5	9.57	1.31	0.959	1.5	3.07	0.017	0.684	0.206
G1–7*	4985	64.07	14.33	5.47	1.67	0.874	1.3	4.01	0.02	0.797	0.223
G1–8*	4985.5	67.18	14.55	3.79	1.46	0.458	1.32	4.08	0.016	0.823	0.19
G1–9*	4986.14	65.02	14.98	4.5	1.5	0.514	1.37	4.16	0.013	0.841	0.224
G1–10*	4987.43	37.42	12.29	4.85	8.32	11.6	0.026	3.74	0.056	0.759	1.01

Note: * data sourced from Gao (2016), Gao et al. (2016).

Table 3
Selected trace and rare earth element concentrations (μg/g) and associated parameters of shales in the Cambrian Qiongzhusi Formation of the deep-water shelf and shallow-water shelf, central Sichuan Basin.

Sample	Depth (m)	B	V	Cr	Co	Ni	Cu	Ga	Rb	Sr	Mo	Ba	U	Th	Sc	Pb	Eu	Sm	Gd	Ba_{bio}	Eu/Eu*
Z2–1	5911.09	98.1	92.8[a]	241[a]	14.1[a]	46.1[a]	26[a]	12.1[a]	73.5[a]	96.8[a]	9.46[a]	907[a]	2.51	5.89	7.06[a]	21.5	1.07[a]	4.75[a]	4.01[a]	630.9	1.1
Z2–3	5912.46	93.6	152[a]	113[a]	21.6[a]	74.1[a]	27.6[a]	11.4[a]	72.9[a]	98.6[a]	15.5[a]	1015[a]	5.46	4.69	6.56[a]	25.9	1.15[a]	5.57[a]	5.58[a]	734.1	1.22
Z2–6	5917.06	101	75.2[a]	178[a]	7.78[a]	24.7[a]	14.5[a]	12.6[a]	78.6[a]	95.7[a]	3.9[a]	786[a]	1.42	5.95	7.47[a]	12.1	1.07[a]	5.31[a]	4.38[a]	496.8	1.07
Z2–10	6324.54	69.3	778	115	12.6	84.2	52.7	13.7	95.6	117	16.5	934	6.94	6.86	8.86	10.4	2.19	11.6	10.6	688.4	1.01
Z2–13	6327.86	91.8	123[a]	101[a]	16.6[a]	93.6[a]	39.9[a]	16.3[a]	106[a]	115[a]	17.6[a]	1051[a]	5.21	5.99	10.7[a]	24.8	1.02[a]	5.05[a]	4.38[a]	762.2	1.05
Z2–14	6328.94	81.6	128	86.2	13.5	57.1	40.7	13.9	97.8	149	40.4	1058	17.7	7.4	10.1	15.4	0.718	4.11	3.7	784.1	1.37
P1–1	5305.74	118	151[a]	208[a]	22.2[a]	56.2[a]	35.7[a]	15.6[a]	83.2[a]	155[a]	10.9[a]	831[a]	3.99	6.04	10.6[a]	16	0.451[a]	2.73[a]	2.41[a]	491	1.19
P1–2	5305.94	114	104[a]	312[a]	10.5[a]	43.9[a]	25.1[a]	13.4[a]	79[a]	107[a]	8.61[a]	1004[a]	2.96	5.53	8.14[a]	14.5	0.49[a]	2.8[a]	2.4[a]	710.8	0.94
P1–8	5585.15	29.6	55.6[a]	58.3[a]	3.78[a]	27[a]	29[a]	3.42[a]	7.76[a]	1047[a]	54.3[a]	1017[a]	80.9	1.23	1.81[a]	22.9	0.317[a]	2.06[a]	2.15[a]	1004	1.1
P1–9	5585.28	57.9	763	148	8.25	90.5	44.5	10.8	84.5	101	15.9	920	7.56	5.13	7.11	10.4	0.946	4.48	3.9	709.8	1.05
P1–15	5589.48	7.23	144[a]	80.2[a]	1.96[a]	20[a]	20[a]	2.65[a]	6.79[a]	535[a]	3.67[a]	324[a]	3.63	1.11	1.62[a]	17.4	1[a]	5.33[a]	4.85[a]	297.2	0.96
P1–17	5590.5	6.74	38.9	58.6	1.6	19	10.3	2.94	14.8	617	1.72	552	1.66	2.13	1.85	18.4	0.99	5.26	4.49	543.8	0.98
A1–1[b]	5028.67	–	87.8	60.5	10.6	37.7	26.3	15.9	79.1	80.5	16.8	1283	10.4	8.45	8.84	30.2	0.825	4.11	3.78	1015	1.14
A1–2[b]	5032.63		144	70.8	12.4	60.2	28.9	16.8	102	70.8	19.9	796	15.2	10.8	11.2	36.9	0.773	3.72	3.19	508.2	0.96
A1–3[b]	5034.27		130	82.4	14	52.1	35.4	18.8	122	66.4	20.4	745	14.8	11.1	11.2	48.9	1.28	4.89	6.06	422.6	1.03
G1–1[b]	4895.99		194	99.7	16.4	93	44.8	23.1	119	113	49.9	740	48.4	12.2	21	62	0.747	4.32	3.16	374.6	0.92
G1–2[b]	4980.87		134	68.5	13.6	64	36.4	16	88	97	21.4	629	17.4	8.97	12.1	43.7	0.983	4.75	3.15	311.9	1.06
G1–3[b]	4981.25		358	78.9	14.6	60.1	32.7	17.4	90.5	90	25.8	559	14.6	9.54	13.7	32.1	2.49	11.6	12.1	243.9	0.92
G1–4[b]	4981.37		159	85.8	17.9	67.5	49.7	19.8	104	111	26.9	695	19.2	11.1	14.1	63.4	3.82	18.2	19	359.1	0.95
G1–5[b]	4983.23		178	81.8	14.8	72.7	38.2	17.7	102	97.7	23	667	14.2	10.6	13.3	59.3	1.26	4.59	3.98	336.5	0.98
G1–6[b]	4983.91		136	75.4	15.7	47.3	42.9	17.5	92	94	51.2	663	22.5	10.7	12.8	58.5	1.02	4.53	3.34	382.3	1.01
G1–7[b]	4985		163	92.3	17.6	59.8	50.6	18.8	110	98.9	23.5	716	15.2	10.7	15.1	80.7	0.851	4.22	3.06	366.2	0.86
G1–8[b]	4985.5		149	91.4	15.4	47.6	46.5	16.4	114	93.5	23.9	763	12.9	11.3	14.3	58.5	0.834	4.36	3.15	407.8	0.82
G1–9[b]	4986.14		178	92.4	17.8	74.4	53.4	17.3	109	87.7	62.2	695	15.3	11.6	14.7	65.4	0.929	4.82	3.81	329.4	0.88
G1–10[b]	4987.43		357	120	14.1	90.6	46.8	20.3	85.3	113	88.1	522	27.2	7.15	7.27	219	0.808	4.01	3.12	222	0.7

Note: [a] data sourced from Zhu et al. (2022). [b] data sourced from Gao (2016), Gao et al. (2016). $Eu/Eu^* = Eu_{PAAS}/(Sm_{PAAS} \times Gd_{PAAS})^{1/2}$ (Shields and Stille, 2001).

n = 14) for well Z2. These values were more negative than those in the SWS (–36.79 ‰ to –29.81 ‰, avg. –32.91 ‰, n = 50) (Fig. 5). Based on the criteria established by Huang (1988) (types I, II_1, II_2, and III are less than –30 ‰, –30 ‰ to –27.5 ‰, –27.5 ‰ to –25 ‰, and greater than –25 ‰, respectively), the OM of the QZS shales was type I. C_{27} dominated the regular steranes, with a range of 37.8 %–53 % (avg. 46 %, n = 3), showing a distribution pattern of $C_{27} > C_{29} > C_{28}$.

4.3. Elemental geochemical analysis

The major element compositions of the QZS shales in the DWS and SWS were similar. The major components were SiO_2 (avg. 57.8 %, DWS; avg. 62.22 %, SWS) and Al_2O_3 (avg. 8.7 %, DWS; avg. 13.22 %, SWS). The CaO and P_2O_5 contents in three samples (P1–8, 1–15, and 1–17) from the DWS were slightly higher than those in the other samples, and the average Ti and Mn contents were 0.64 % and 0.08 %, respectively (Table 2). Compared with the post-Archean Australian shale (PAAS) (Taylor and McLennan, 1985), some of the elements, such as Ca, Mg, Na, and P, were obviously enriched (Fig. 6A). Large amounts of TE, such as U, Mo, Sr, V, Ni, and Ba, were widely enriched in the QZS shales (Table 3). The total TE ranged from 1188.08 to 3561.63 μg/g (avg. 2007.1 μg/g, n = 12) in the DWS and from 1325.5 to 2797.4 μg/g (avg. 1765.5 μg/g, n = 13) in the SWS. Compared with those in the PAAS (Taylor and McLennan, 1985), some elements, such as V, Mo, U, Ni, Ba, and Pb, were enriched (Fig. 6B). The Eu/Eu* content in the DWS shales ranged from 0.94 to 1.37 (avg. 0.747), which is higher than that in the SWS (0.70–1.14, avg. 0.94) (Table 3; Fig. 13B).

5. Discussion

5.1. Stratigraphic sequence

The QZS shales are unconformably located at the top of the carbonate system in the Dengying Formation (Fig. 1B) (Zou et al., 2014), as characterized by high gamma-ray logging response (Gao et al., 2016). Xu et al. (2011) used Re–Os isochron dating and determined that the age of the Ni–Mo ore layer at the bottom of the QZS was 521 ± 5 Ma. The thickness distribution of the QZS is controlled by the evolution of the Deyang–Anyue rift trough and paleogeomorphology (Wei et al., 2017). Generally, the Mn/Fe ratio in deep-sea sediments is higher than that in shallow sediments, which is primarily because Mn compounds are more stable than Fe. However, calcium and magnesium mainly occurred in carbonate. (Al + Fe)/(Ca + Mg) decreased gradually as the water depth increased and because of the lack of terrigenous materials (Zhang et al., 2017). Compared with the SWS, the shales in the DWS formed at a greater water depth (Fig. 7).

A large-scale transgression occurred during the deposition of the QZS, and it was accompanied by a relatively strong filling effect (Song, 1996). Therefore, the total thickness of the DY and QZS varies slightly in the planar direction, thus reflecting the controlling effect of the accommodation space along the distribution (Song, 1996). Globally, a rapid increase in sea level occurred immediately after the end of the Precambrian, and it lasted for approximately 1–1.5 million years and then decreased slightly, experiencing multiple up-and-down cycles (Haq and Schutter, 2008). A detailed analysis of the sedimentary characteristics revealed that the V–Ni-enriched polymetallic layer at the bottom of the QZS may be the maximum flooding surface (Yeasmin et al., 2017). From the bottom to the top layer, the sediment-detrital fluxes (shale to siltstone) increased in stages, suggesting that the transgression began in the Early Cambrian (Zhao et al., 2020a) with a rapid increase in the sea level and then in decline slowly in stages. During the Early Cambrian, the structure in the DWS was slightly lower than that of the SWS (Gaoshiti–Moxi), which caused the thickness of the QZS to gradually increase from the SWS to the north and northwest (Ma et al., 2020; Zhao et al., 2020b) (Fig. 1C). The thicknesses of the QZS in wells Z2 and P1 were 700 and 510 m, respectively, whereas the thickness in wells G1 and

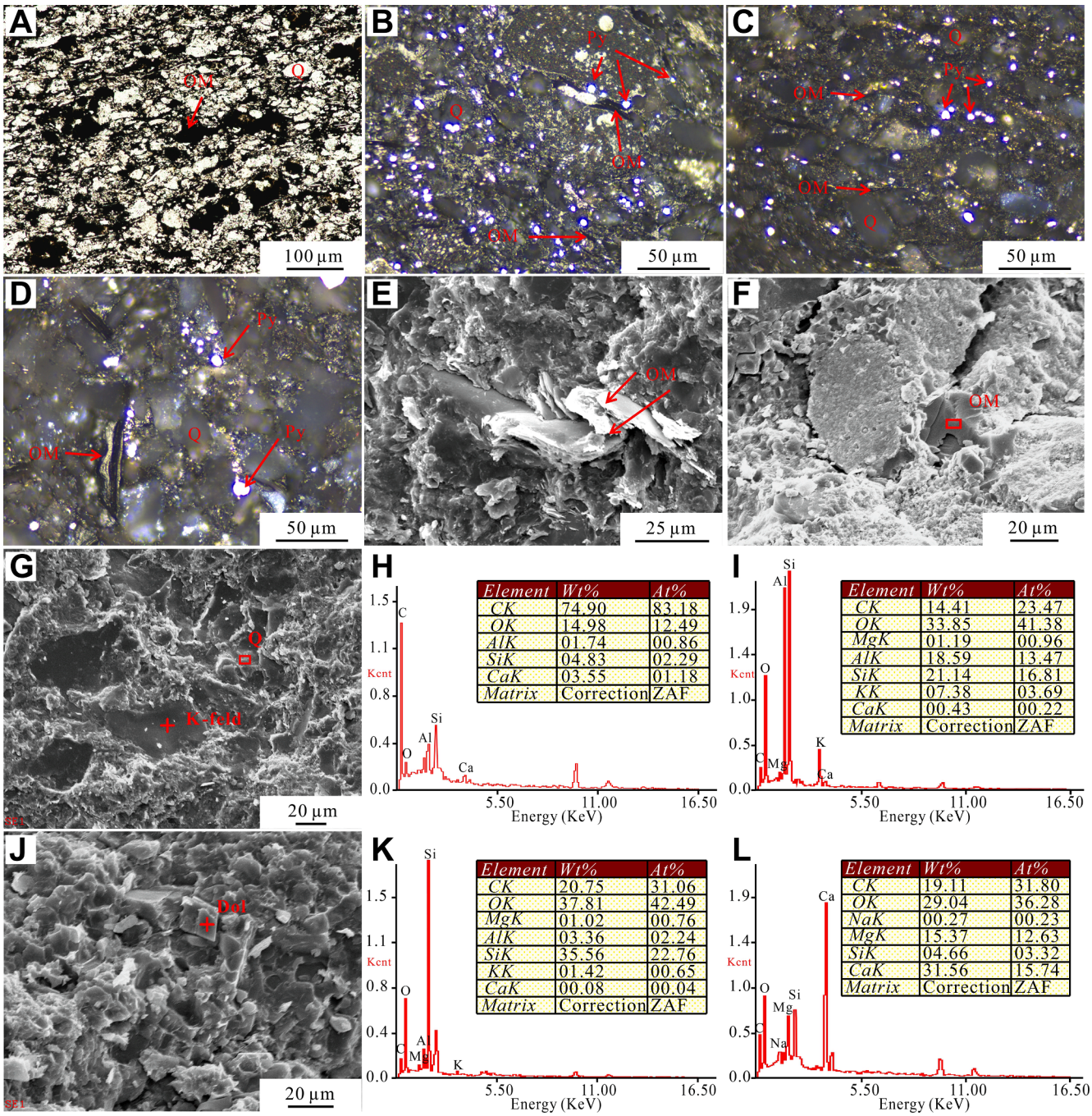

Fig. 2. Microphotographs of shales in the Cambrian Qiongzhusi Formation of the deep-water shelf, central Sichuan Basin. (Note: PPL, plane-polarized light; ORL, oil-immersion reflected light; OM, organic matter; Py, pyrite; Q, quartz; K-feld, K-feldspar; Dol, dolomite). (A) PPL: quartz and OM in shale, P1–9. (B) ORL: banded OM at the edge of quartz, and pyrite with high reflective brightness, P1–9. (C) ORL: pyrite and banded OM, mainly circular quartz, Z2–11. (D) ORL: pyrite and banded OM, mainly quartz, Z2–8. (E) Scanning electron microscopy (SEM) image of OM, Z2–11. (F) SEM image of OM, P1–9. (G) SEM image of K-feldspar and quartz, Z2–11. (H) Energy dispersive X-ray spectrometer (EDS) data of OM in Fig. 2F. (I) EDS data of K-feldspar in Fig. 2G. (J) SEM image of dolomite, P1–9. (K) EDS data of quartz in Fig. 2G. (L) EDS data of dolomite in Fig. 2J.

A1 in the SWS was only approximately 200 m. The results indicated that high-quality and thicker deposits developed in the DWS and deep basinal regions.

5.2. Sedimentary environment of the deep-water shelf and shallow-water shelf

5.2.1. Paleoclimate

The paleoclimate primarily affects OM accumulation by influencing the weathering and transformation degree of unstable materials in sediments (Leythaeuser, 1973; Müller and Suess, 1979). The C-value, chemical index of alteration (CIA), and Sr/Cu ratio have been proposed to characterize the climatic conditions (Moradi et al., 2016; Nesbitt and Young, 1982; Zhao et al., 2007). The C-value is obtained by Σ (Fe + Mn + Cr + Ni + V + Co)/Σ (Ca + Mg + Sr + Ba + K + Na), and it is generally accepted that Fe, Mn, Cr, Ni, V, and Co are more advantageous and abundant than Ca, Mg, K, Na, Sr, and Ba under humid conditions (Moradi et al., 2016; Tan et al., 2019). Furthermore, the CIA can be obtained as follows: $100 \times Al_2O_3/(Al_2O_3 + CaO^* + Na_2O + K_2O)$, where CaO* is the CaO content incorporated in the silicate fraction (Nesbitt

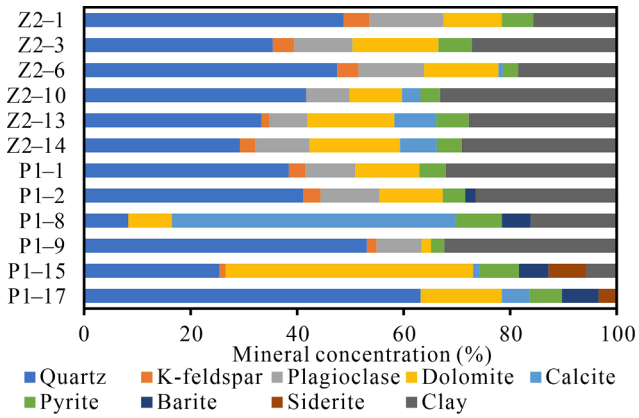

Fig. 3. Mineral compositions (%) of shales in the Cambrian Qiongzhusi Formation of the deep-water shelf, central Sichuan Basin.

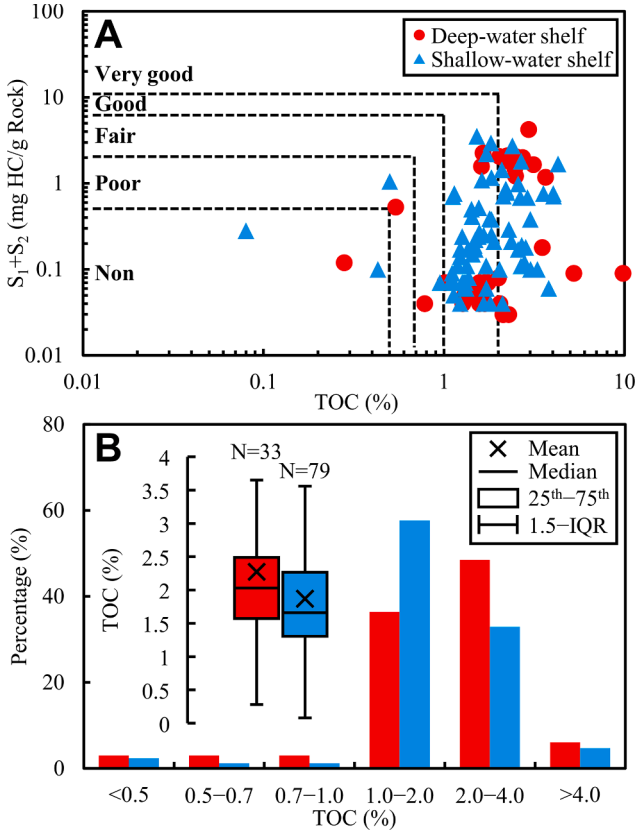

Fig. 4. Correlation diagrams between (S_1 + S_2) and the total organic carbon (TOC) content (A) and TOC distribution histogram (B) of shales in the Cambrian Qiongzhusi Formation of the deep-water shelf and shallow-water shelf, central Sichuan Basin. Baseline reference from Peters (1986) and Li et al. (2021). Data for the QZS shales in the shallow-water shelf were sourced from Gao et al. (2016), Li et al. (2021), Shi et al. (2018), and Wang et al. (2019).

and Young, 1982). CaO* can also be represented by CaO – P_2O_5 × 10/3 when the carbonate content is low (Tan et al., 2019). In general, a C-value of > 0.4 represents a semiarid to subhumid environment, whereas a Sr/Cu ratio of < 5 represents a humid environment (Hakimi et al., 2017). The higher the C-value and CIA values are, the lower the Sr/Cu ratio and the more humid the paleoclimatic conditions (Hakimi et al., 2017; Zhao et al., 2007). Al and Ga are predominant in kaolinite formed under humid and warm conditions, whereas K and Rb are related to illite formed in cold and arid climates (Beckmann et al., 2005; Hieronymus et al., 2001).

The provenance of the QZS is predominantly intermediate igneous rocks (Fig. 8A). According to the chart reported by Roy and Roser (2013), the shales in the two shelf conditions share a similar overall humid background (Fig. 9), and part of the DWS shales represents semiarid paleoclimate. Generally, a more humid climate corresponds to a higher chemical weathering intensity (positive correlation), and the QZS shales in the study area also reflect this covariant feature (Fig. 9). Specifically, the C-value of the shales in the DWS was 0.02–0.58 (avg. 0.34) and the Sr/Cu ratio was 2.22–59.9 (avg. 13.02). Excluding three values>10 (P1–8, 1–15, and 1–17), the mean Sr/Cu ratio was 3.73. In summary, the C-value of the QZS shales in the DWS was slightly lower than that in the SWS (0.21–1.29, avg. 0.49), whereas the Sr/Cu ratio was higher (1.64–3.06, avg. 2.33). Most of the samples exhibit Sr/Cu values of<5, which is also consistent with the findings of Wang et al. (2020). Hence, the paleoclimate was slightly more humid in the SWS.

5.2.2. *Paleosalinity*

Salinity can be evaluated using the Sr/Ba and B/Ga ratios (Wei and Algeo, 2020). The main sources of Sr in the ocean are river inflow, seafloor hydrothermal processes, and carbonate dissolution (Godderis and Veizer, 2000). A higher Sr/Ba ratio corresponds to higher salinity of the sedimentary water mass (Zhang et al., 2018). The residence time of Sr (2.4 Myr) is longer than the mixing time in oceans (1.5 Kyr) (Krabbenhöft et al., 2010), whereas the residence time of Ba in oceans is relatively short (11 Kyr) (Allmen et al., 2010). B has a longer residence time in oceans (20 Myr) (Wei and Algeo, 2020), and its concentration in anoxic water is greater than that in oxidized water (Kulinski et al., 2017). Ga is mainly derived from the weathering of quartzose and feldspathic silicate minerals (Shiller and Frilot, 1996). Higher B concentrations in seawater and the rapid B uptake by sediments in alkaline porewaters result in higher B/Ga ratios in oceans (Wei and Algeo, 2020). Based on the aforementioned principles, Wei and Algeo (2020) established a salinity proxy based on the B/Ga relationship, and the B/Ga ratios of fresh, blackish, and marine water are < 3, 3–6, and > 6, respectively.

B/Ga values of 2.29–8.64 in the QZS shales in the DWS (avg. 6.33) reflect medium to high salinity characteristics. The Sr/Ba ratio in the DWS (0.10–1.54, avg. 0.41) was significantly higher than that of the SWS (0.06–0.22, avg. 0.14), indicating that the salinity of the lower structural positions was higher than that of the shallow positions. Wang et al. (2020) studied the QZS shales in the Ziyang–Weiyuan area with a similar DWS background based on the gammacerane index and β-carotene contents, and they also concluded that the paleosalinity of the waterbody in the DWS was higher than that in the SWS.

5.2.3. *Primary productivity*

Primary productivity serves as an important material basis for evaluating the degree and scale of the original OM enrichment (Chen et al., 2020; Schoepfer et al., 2015; Shen et al., 2014), and it is usually assessed using the TOC, P, Ti, Cu, and Ba contents (Calvert and Pedersen, 2007; Chen et al., 2020; Schoepfer et al., 2015; Shen et al., 2014, 2015; Tribovillard et al., 2006). The residual TOC content may be affected by OM dilution and the preservation conditions during deposition; however, it is still a direct indicator of primary productivity (Canfield, 1994; Pedersen and Calvert, 1990). The residence time of Ba in seawater is relatively short, and Ba_{bio} is mainly derived from barite in sediments (most of the barite sinks to the sediment–water boundary). Ba_{bio} is considered a favorable proxy for productivity because of its stability and high burial efficiency (Bąk,2007; Dymond et al., 1992; Schoepfer et al., 2015). The average TOC content of the QZS shales in the DWS was significantly higher than that of the SWS (Fig. 4B). The relatively higher TOC content indicates that the DWS tends to have higher productivity than the SWS. The ratio of nutrient elements (P) to terrestrial supplies (Al and Ti) also showed a trend of higher productivity in the DWS (Fig. 10A).

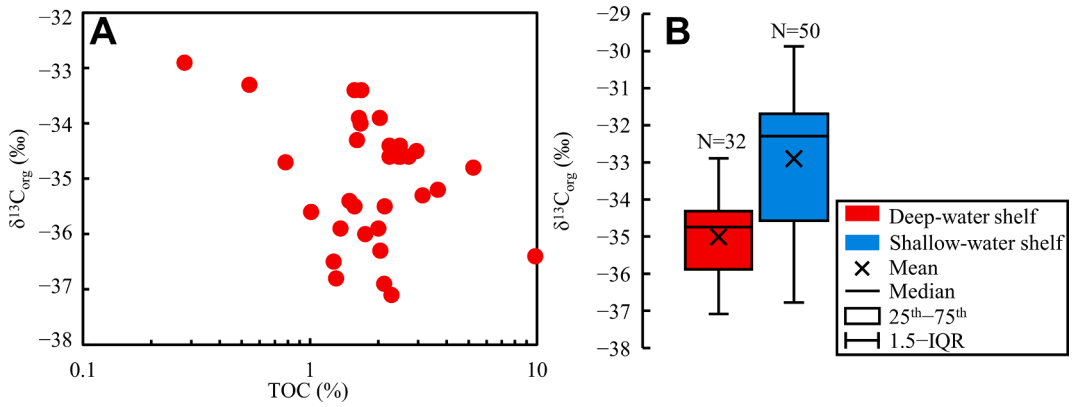

Fig. 5. Organic carbon isotope ($\delta^{13}C_{org}$) versus the total organic carbon (TOC) content of shales in the Cambrian Qiongzhusi Formation of the deep-water shelf (A) and $\delta^{13}C_{org}$ distribution in different shelf conditions, central Sichuan Basin (B). Data of the QZS shales in the shallow-water shelf were sourced from Gao et al. (2016), Shi et al. (2018), and Wei et al. (2015).

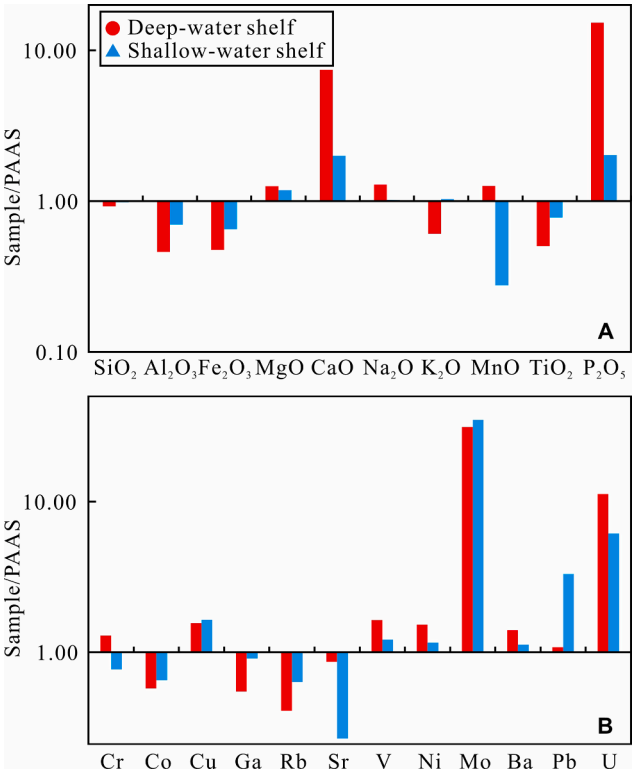

Fig. 6. PAAS-normalized concentrations of major and trace elements of shales in the Cambrian Qiongzhusi Formation of the deep-water shelf and shallow-water shelf, central Sichuan Basin.

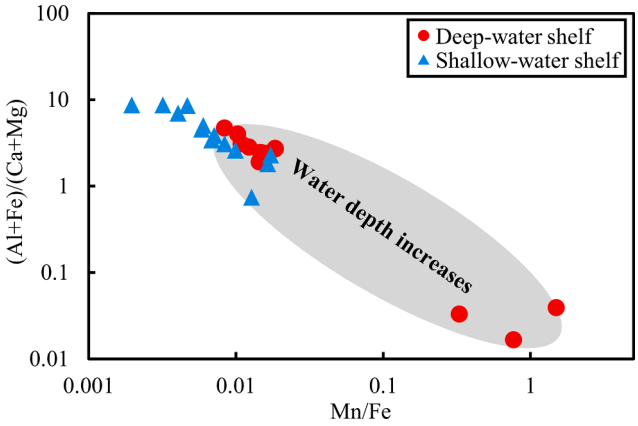

Fig. 7. Mn/Fe versus (Al + Fe)/(Ca + Mg) ratios of shales in the Cambrian Qiongzhusi Formation of the deep-water shelf and shallow-water shelf, central Sichuan Basin.

Ba_{bio} is calculated as follows: $Ba_{bio} = Ba_{total} - Al \times (Ba/Al)_{detr}$, where Ba_{total} is the total Ba and Ba_{detr} represents the detrital origin. A method for estimating Ba_{detr} based on the intersection of Al and Ba was proposed by Rutsch et al. (1995) and Shen et al. (2015), in which the sample with the lowest Ba/Al ratio does not contain biological Ba. The $(B/Al)_{detr}$ value of the QZS shales in the SWS (0.0046) reported by Gao et al. (2016) was used in this study. The Ba_{bio} values of the QZS shales ranged from 222 to 1014.5 μg/g (avg. 406.1 μg/g) in the SWS and from 297.2 to 1003.5 μg/g (avg. 654.4 μg/g) in the DWS (Fig. 10B–C). Yan et al. (2015a) analyzed the primary productivity of the Silurian Longmaxi Formation (LMX) shales in South China based on the Ba_{bio} values. The productivity of the LMX shales was found to be medium to high (443.39–2009.04 μg/g, avg. 1191.95 μg/g, n = 27) (Yan et al., 2015a). The Ba_{bio} values of the QZS shales were lower than those of the LMX shales, indicating relatively low to medium productivity.

Based on an empirical formula suitable for marine paleoproductivity reported by Müller and Suess (1979), the primary production values of the QZS shales were 89.9–299.4 (avg. 150.94 $gC{\cdot}m^{-2}{\cdot}kyr^{-1}$) and 54.4–95 $gC{\cdot}m^{-2}{\cdot}kyr^{-1}$ (avg. 71.45 $gC{\cdot}m^{-2}{\cdot}kyr^{-1}$) in the DWS and SWS, respectively (Fig. 10B), which were lower than the high productivity values obtained for the California coast (avg. 255.2 $gC{\cdot}m^{-2}{\cdot}kyr^{-1}$), the Indian Ocean monsoon circulation zone (avg. 232.2 $gC{\cdot}m^{-2}{\cdot}kyr^{-1}$), the Northwest Arabian upwelling sea (avg. 394.2 $gC{\cdot}m^{-2}{\cdot}kyr^{-1}$) (Dunne et al., 2005; Schoepfer et al., 2015), and the Chile-Peru coast (avg. 2511.9 $gC{\cdot}m^{-2}{\cdot}kyr^{-1}$) based on satellite estimates (Longhurst et al., 1995; Shen et al., 2015). These findings also indicate that the primary productivity of the QZS shales is at a low to medium level. Interestingly, the QZS shales in the DWS had higher primary productivity (for detailed discussion, see Section 5.3.1).

5.2.4. *Redox conditions*

The correlation ratio of TE has been widely used to determine redox conditions (Algeo and Liu, 2020; Algeo and Tribovillard, 2009; Jones and Manning, 1994; Rimmer, 2004; Tribovillard et al., 2012). Jones and Manning (1994) first proposed U/Th, V/Cr, and Ni/Co standards to distinguish the redox environment. U/Th, V/Cr, and Ni/Co ratios of < 0.75, <2, and < 5, respectively, represent an oxic condition; ratios of 0.75–1.25, 2–4.25, and 5–7, respectively, represent suboxic conditions; whereas ratios of > 1.25, >4.25, and > 7, respectively, represent suboxic to euxinic conditions. A high V/(V + Ni) ratio indicates anoxic

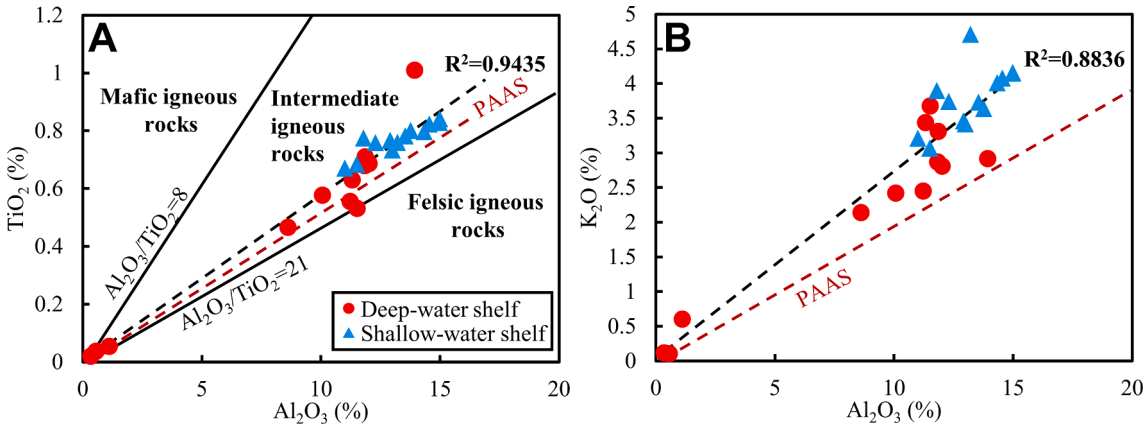

Fig. 8. Al_2O_3 versus TiO_2 (A) and K_2O contents of shales in the Cambrian Qiongzhusi Formation of the deep-water shelf and shallow-water shelf, central Sichuan Basin. Baseline reference from Hayashi et al. (1997).

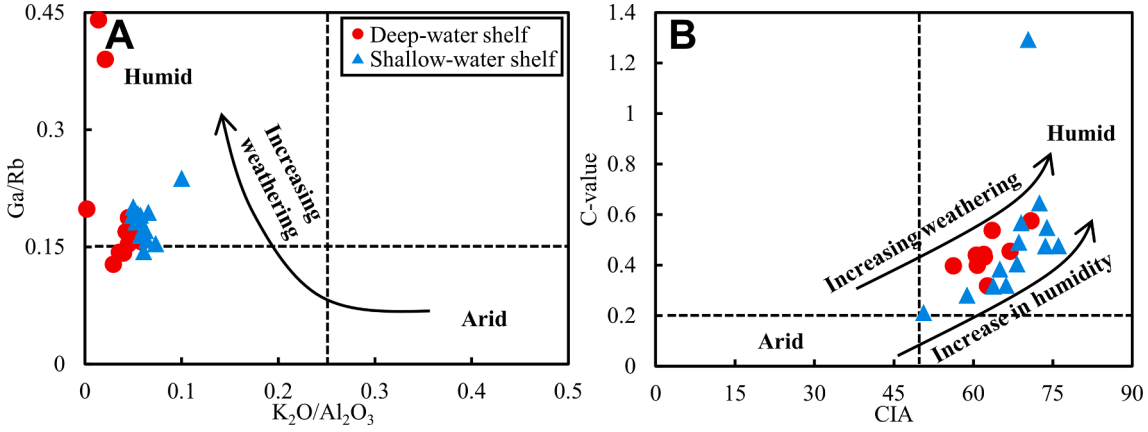

Fig. 9. Correlation diagrams between the K_2O/Al_2O_3 and Ga/Rb ratio (A) and the chemical index of alteration (CIA) and C-values (B) of shales in the Cambrian Qiongzhusi Formation of the deep-water shelf and shallow-water shelf, central Sichuan Basin. Baseline references from Nesbitt and Young (1982), Roy and Roser (2013), and Zhao et al. (2007).

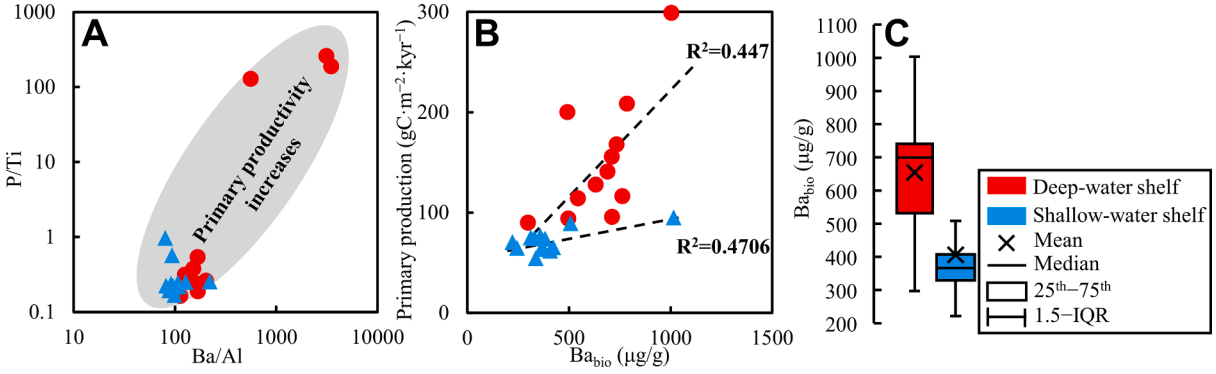

Fig. 10. Correlation diagrams between the Ba/Al and P/Ti ratios (A), primary production (B), and Ba_{bio} distribution histogram (C) of shales in the Cambrian Qiongzhusi Formation of the deep-water shelf and shallow-water shelf, central Sichuan Basin.

conditions, while a low value indicates a dysoxic to oxidation redox environment (Lewan, 1984). Hatch and Leventhal (1992) established that V/(V + Ni) ratio values of < 0.46 represent an oxic environment, 0.46–0.6 represent a dysoxic environment, 0.54–0.82 represent an anoxic environment, and ratios > 0.84 represent a euxinic environment and strongly restricted water for fine-grained sediments.

For shale, the latest research reflects that enrichment factors (EFs) are more useful as indicators of a redox condition (Algeo and Liu, 2020; Algeo and Tribovillard, 2009; Tribovillard et al., 2012). U^{4+} is insoluble in a reducing environment, whereas Mo enrichment requires a greater reduction of H_2S in euxinic water (Helz et al., 1996). Simultaneously, Mo can be scavenged by metal oxyhydroxides by accelerating the adsorption of molybdate, resulting in the formation of particle shuttles (Algeo and Tribovillard, 2009). In this mechanism, Mo initially increases rapidly and becomes greater than U (Fig. 11). Mo-EF and U-EF gradually increase in equal proportions after the EF reaches 10 and finally converge to the unrestricted marine boundary of euxinic water (Algeo and Liu, 2020; Tribovillard et al., 2012).

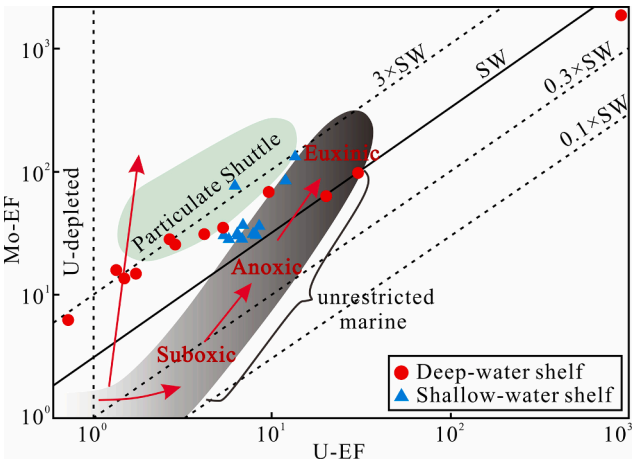

Fig. 11. Covariation of uranium and molybdenum enrichment factors (U-EF and Mo-EF) of shales in the Cambrian Qiongzhusi Formation of the deep-water shelf and shallow-water shelf, central Sichuan Basin. X-EF = $(X/Al)_{Sample}/(X/Al)_{PAAS}$, where $(X/Al)_{Sample}$ represents the contents of trace elements and $(X/Al)_{PAAS}$ represents the data from the post-Archean Australian shale (PAAS) (Taylor and McLennan, 1985).

The geological conditions in the study field, including the different OM sources and TE enrichment, different types and relative quantities of OM, and mixing degree of marine and terrigenous facies, impose restrictions on the application of a fixed threshold (Rimmer, 2004). Therefore, a reasonable and reliable conclusion can be obtained by using multiple indicators. Kimura and Watanabe (2001) studied the PC–C boundary and concluded that it consists of a widespread anoxic environment. The U-EF and Mo-EF contents of the QZS shales in the SWS were found to be 5.4–19.7 and 28.8–135.4, respectively (Fig. 11), which are close to the ratio of 1–3 × SW. This indicates that the QZS shales were deposited in an anoxic–euxinic environment (Gao et al., 2021; Tribovillard et al., 2012; Wang et al., 2020). Moreover, the V/(V + Ni) ratios ranged from 0.68 to 0.86 (avg. 0.73) (Fig. 12), thus revealing that the QZS in the SWS formed in an anoxic–euxinic condition (Hatch and Leventhal, 1992; Rimmer, 2004).

The U-EF and Mo-EF contents of the QZS shales in the DWS had a large span, with one sample in the range of 0.1–1 × SW (P_2O_5 rich, P1–8). The distribution of the remaining samples resembled that of the SWS (Fig. 11). The V/(V + Ni) ratios of the shales ranged from 0.57 to 0.9 (avg. 0.73), and based on the threshold established by Hatch and Leventhal (1992), one sample (Z2–13) was classified as being in a dysoxic environment while the rest of the samples were generally divided into anoxic to euxinic conditions. $\delta^{13}C_{org}$ values can also be used to analyze the redox conditions of sedimentary water masses (Guo et al., 2007; Lewan, 1986; Tostevin et al., 2016). The $\delta^{13}C_{org}$ values of the QZS shales in the DWS were lower than those in the SWS, indicating that the conditions were more euxinic in the overall suboxic background of the SWS (Fig. 5B). In addition, the distribution of the V/(V + Ni) (>0.85) and V/Sc (>80) ratios in the DWS region was higher than that in the SWS shales (Fig. 12A, C), which is similar to that of the Th/U ratio (Fig. 12B). This finding suggests that the QZS shales in the DWS region formed in a more reductive environment.

5.2.5. *Terrigenous flux*

The degree of terrigenous detritus inputs may impact OM enrichment (Ibach, 1982). Ibach (1982) found that when the deposition rate remained constant, from calcareous to black shale, the organic content gradually increased. For each lithology, increasing the deposition rate

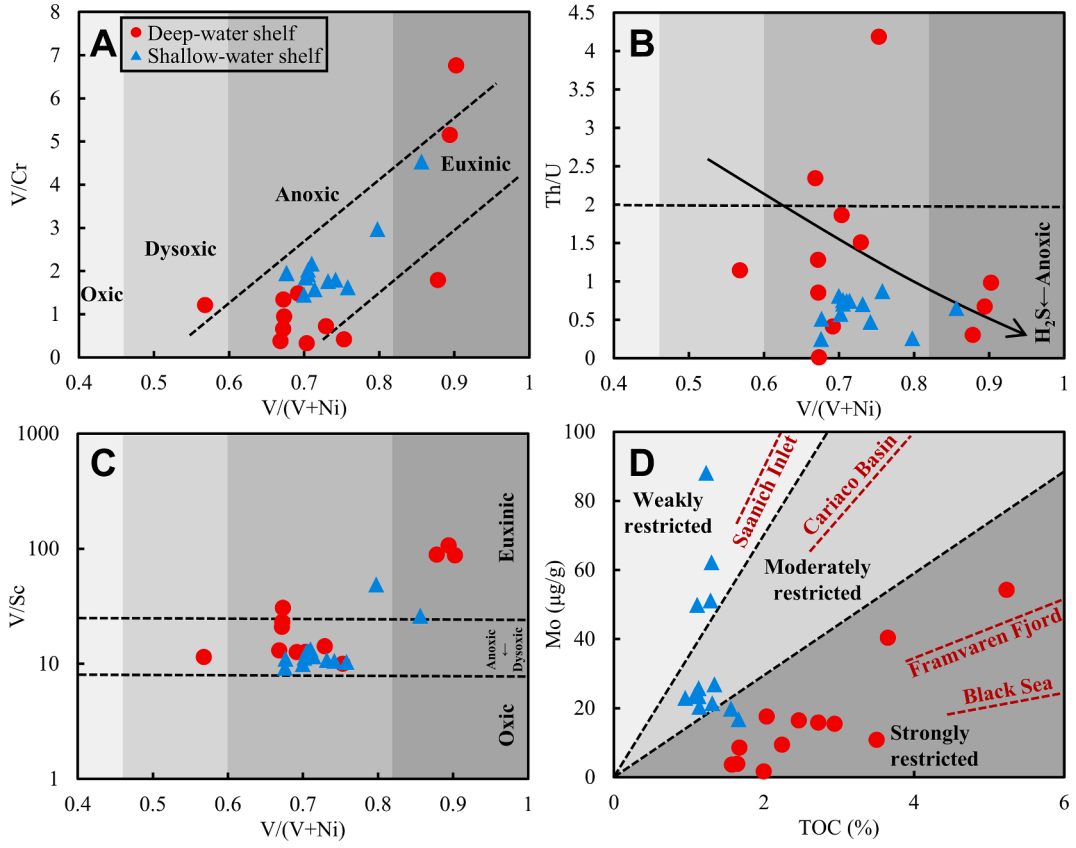

Fig. 12. Correlation diagrams between the V/(V + Ni) and V/Cr ratios (A), Th/U (B), V/Sc (C), and TOC versus Mo contents (D) of shales in the Cambrian Qiongzhusi Formation of the deep-water shelf and shallow-water shelf, central Sichuan Basin. Baseline in the figures taken from Algeo and Lyons (2006), Jones and Manning (1994), Kimura and Watanabe (2001), and Wignall and Twitchett (1996).

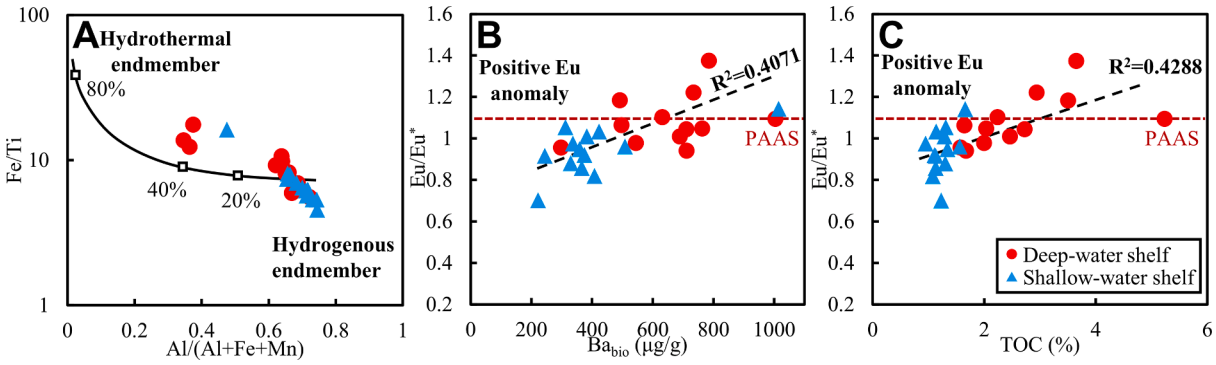

Fig. 13. Proportions of hydrothermal activities and their impact on primary productivity under different shelf conditions, central Sichuan Basin. (A) Al/(Al + Fe + Mn) versus Fe/Ti (Marchig et al., 1982; Tan et al., 2021). (B) Ba_{bio} versus Eu/Eu*. (C) Ba_{bio} versus TOC.

had a twofold effect on the OM contents. First, as the deposition rate increases, the TOC content increases due to the reduction in near-surface microbial degradation. At a higher deposition rate, clastic dilution will reduce the OM content. Detritus input may dilute OM adsorption processes to aluminosilicates (Rimmer et al., 2004) or affect the burial rates and preservation integrity of OM (Canfield, 1994). Because Al is mainly present in clay minerals while Ti is found in clay, sand, and other particles, Ti/Al ratios have been widely used in the evaluation of terrigenous flux (Bertrand et al., 1996; Murphy et al., 2000; Rimmer et al., 2004; Yan et al., 2015b; Xiao et al., 2021; Zhang et al., 2018). Higher Ti/Al ratios indicate larger particles and higher deposition rates.

The Ti/Al ratios of the QZS shales in the DWS and SWS exhibited ranges of 0.05–0.08 (avg. 0.065) and 0.05–0.07 (avg. 0.066), respectively (Table 2; Fig. 15F). The deposition rate of the QZS shales was higher than that of the LMX shales in South China (mean Ti/Al = 0.058) (Yan et al., 2015a). Over approximately 20 million years, the formation thickness of the QZS was approximately 90–700 m (from well G1 to well Z2), and the estimated deposition rate was approximately 0.45–3.5 cm/Kyr. A higher deposition rate corresponds to higher TOC value of the fine-grained sediments (Hofmann et al., 2000). Furthermore, the Al content of the QZS shales was strongly correlated with the Ti and K contents (R^2 = 0.9435 and 0.8836, respectively) (Fig. 8), indicating that the debris supply was generally homogeneous (Yan et al., 2015b).

5.3. *Unique watermass response in the deep-water shelf*

5.3.1. *High primary productivity advantage*

A comprehensive analysis based on the TOC, primary production, and Ba_{bio} values revealed that the primary productivity of the QZS shales in the DWS was higher (higher TOC, primary production, and Ba_{bio}; Canfield, 1994; Pedersen and Calvert, 1990; Schoepfer et al., 2015) (Fig. 10). The water depth of the DWS during the Cambrian was greater than that of the SWS (Fig. 1C; Fig. 7). Under the same biorich zone, a greater depth of the water mass results in higher biomass. More biomass provides the basic material conditions for the formation of OM, thereby increasing its productivity. Moreover, strike-slip faults were widely developed in the Sinian–Cambrian System in the Sichuan Basin and were active during the Cambrian (Ma et al., 2018). Hydrothermal fluids migrated onto the submarine surface through these active strike-slip faults and were wide spread in the Yangtze Region (Zhang et al., 2021a). Hydrothermal fluids brought mantle and crust material and provided essential nutrients (e.g., Fe, Mn, Cu, Zn, and Ni) (Korzhinsky et al., 1994), thereby supplementing the elements with reduced concentration consumed for biological growth (such as ammonia, nitrate, and dissolved silicon) (Dugdale, 1972; Korzhinsky et al., 1994). At the same time, these fluids promoted the reproduction of organisms (Jones, 1978) (e.g., N and Si supplementation is beneficial for the growth rate of marine biomass such as diatoms; Dugdale, 1972; Ryther and Dunstan, 1971). The increased growth rate of plankton promotes the metabolic rate and total flux of organisms, thereby increasing productivity (Dick et al., 2013; Pang et al., 2022; Pašava et al., 2021; Wu et al., 2020). McKibben and Williams (1990) proposed that the biological productivity in hydrothermal active zones would be 1–3 times higher than that in normal ocean conditions. Similarly, studies on the Niutitang (equivalent to the QZS shales) (Awan et al., 2020) and Datangpo Formation shales in South China (Tan et al., 2021) and the Yuertusi Formation shales (Zhang et al., 2020) in the Tarim Basin in Western China have shown that extensive transgression and hydrothermal upwelling could significantly increase productivity. Moreover, the main factor for OM enrichment in sediments (TOC > 12.54 %) of the Peruvian Basin is the high primary productivity resulting from upwelling (Suess and Thiede, 2013).

Hydrothermal activities are typically characterized by a positive Eu anomaly (Peter and Goodfellow, 1996). Simultaneously, a high Fe/Ti ratio and low Al/(Al + Fe + Mn) contents indicate the presence of hydrothermal activities owing to the high Fe and Mn contents in the hydrothermal fluids (Marchig et al., 1982). Generally, DWS sites are usually a target for the enrichment and unloading of hydrothermal upwelling (Wu et al., 2020). The local disturbance of the water mass caused by upwelling will promote biological activity and thus increase its metabolic rate (Pašava et al., 2021). We found a significantly positive correlation between the Eu/Eu* and TOC (R^2 = 0.4288) and the productivity indicator (Ba_{bio}) (R^2 = 0.4071), which also confirmed that upwelling caused by submarine hydrothermal activities during the formation of the QZS shales increased the primary productivity (Fig. 13).

5.3.2. *Restricted and high salinity water conditions*

The Mo/TOC ratios reflect hydrological information of the sedimentary water masses. Based on the Mo and TOC values of five typical regions, Algeo and Lyons (2006) established criteria for the degree of water mass restriction, i.e., the Mo/TOC ratios of weakly, moderately, and strongly restricted water mass are > 35, 5–15, and < 15, respectively. In highly anoxic to euxinic waterbodies, the subsequent supply of Mo is limited, which causes Mo to be gradually undermined by sediments and thus getting depleted.

Based on data of the QZS developed in the SWS position (Gaoshiti–Moxi area) reported by Gao et al. (2016), it was concluded that the Mo/TOC values of the shales in the DWS (0.86–11.07, avg. 5.50) were much lower than those in the SWS (10.12–71.63, avg. 28.56) (Fig. 12D), reflecting strongly restricted water conditions in the DWS (Algeo and Lyons, 2006). More specifically, fine-grained sediments developed in the deep-slope region hindered the subsequent supply of Mo because of the deeper sedimentary water mass. Therefore, the Mo content in the DWS (1.72–54.3, avg. 16.54) was significantly lower than that in the SWS (16.8–88.1, avg. 34.85) (Fig. 12D). The degree of secondary material exchange in the deep stagnant waterbody was low, and the euxinic zone was more likely to develop in the DWS.

Wang et al. (2019) performed TE, biomarker, and fossil analyses of

the QZS shales in the Ziyang–Weiyuan area and found that the shales exhibit strong reducing conditions and high salinity water characteristics. Based on the Sr/Ba ratios (avg. 0.41, DWS; avg. 0.14, SWS), the DWS had a higher salinity condition. Based on simulation experiments, Zhang et al. (2021b) found that the C_{27}–C_{28}–C_{29} regular sterane ternary diagrams still inherited the genetic characteristics of the original OM and could effectively indicate the OM input, even under the high maturity settings. The relative C_{27}–C_{28}–C_{29} content reflects the OM origin of the QZS shales, with plankton and bacteria being its parent genetic material (Adegoke et al., 2014; Huang and Meinschein, 1979) (Fig. 14). The OM of the deep anoxic to euxinic water layer in the QZS mainly stemmed from α-Proteobacteria (negative $\delta^{13}C_{org}$ values), whereas the OM in the SWS was mainly derived from chlorophytes, pelagophyceae, and cyanobacteria (Wang et al., 2019). Fang et al. (2019) analyzed the Ediacaran–Lower Cambrian shale and found that algae are the main source of OM in platform facies (SWS) while chemoautotrophic and methanotrophic biomass are the main sources of OM in deep basinal water. Comprehensive analysis reveals that the shales in the DWS had higher paleosalinity, strongly restricted water mass, and higher primary productivity.

5.4. OM enrichment process

OM enrichment is caused by a combination of paleowater conditions, paleoclimate conditions, productivity supply, and preservation conditions (Lash and Blood, 2014; Müller and Suess, 1979; Pedersen and Calvert, 1990; Xiao et al., 2021). However, owing to the different contributions or degrees of influence of the various control factors, one or more factors become the main control factors of OM enrichment in a specific region. For example, the deposition rate needs to be considered only when it varies considerably from the deposition TOC content. Müller and Suess (1979) observed that when the deposition rate is low, OM enrichment is positively correlated with the deposition rate, whereas when the deposition rate exceeds the critical value, OM is diluted and diminished with an increase in the deposition rate. Simultaneously, a stable water mass condition is conducive to OM enrichment and deep reducing water facilitates OM preservation (Henrichs and Reeburgh, 1987; Leythaeuser, 1973; Müller and Suess, 1979). Primary productivity is the basis of OM enrichment fluxes and often controls the TOC content in shale sediments, together with redox conditions

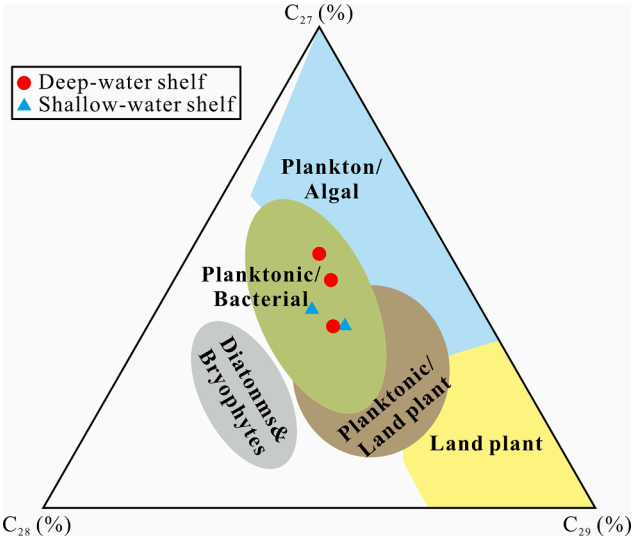

Fig. 14. Ternary diagram of C_{27}, C_{28}, and C_{29} steranes of shales in the Cambrian Qiongzhusi Formation (QZS) showing the source of organic matter under different shelf conditions, central Sichuan Basin. Baseline in the figures reference from Adegoke et al. (2014). Data for the QZS shales in the shallow-water shelf (wells A1 and G1) were sourced from Wang et al. (2019).

(Hofmann et al., 2000). During the short depositional period of the QZS, large-scale transgression filled the carbonate platform, DWS, and SWS area of the Dengying Formation. A rise in sea level increases the development of OM, such as algae and deep-water chemoautotrophic and methanotrophic biomass bacteria, in the DWS. The QZS shales content of the central Sichuan Basin correlates best with the productivity proxy (Ba_{bio}) ($R^2 = 0.447$), while the correlations with other geological conditions are low, reflecting the characteristics of multifactorial joint participation and productivity domains (Fig. 15).

Owing to the larger sedimentary capacity space, hydrothermal upwelling, and more restricted water mass conditions, the DWS had higher productivity than the SWS, which provided the basic conditions for the formation of high-quality shale in the DWS. The climate during this period was overall humid and the evaporation of water was limited, thus avoiding the formation of gypsum and ultra-high salinity waterbody. Fresh water may also infiltrate the ocean's surface layer to reduce salinity under humid conditions, thereby enabling numerous types of organisms to thrive in the surface layer (Wang et al., 2020). Increased terrigenous input and deposition rates can carry nutrients, reduce near-surface microbial degradation, and enhance productivity (Hofmann et al., 2000; Ibach, 1982). Moreover, when further escalations occur, they usually result in OM dilution. Water turbulence deteriorates preservation conditions and reduces productivity (Canfield, 1994; Rimmer et al., 2004). The deposition rate of the QZS shales in the study area is moderate, which is less than the threshold value (5 cm/Kyr) reported by Tyson (2001). Therefore, the deposition rate and terrigenous input of the QZS shales have a positive effect on OM enrichment, which can also be seen in Fig. 15F.

Under the background of rapid deposition, many algae died and fell into the depositional interface. This process also led to the depletion of the inorganic carbon pool dissolved in water, resulting in a higher degree of anoxia and restriction of the water mass (Jiang et al., 2007). The paleosalinity also increases under the condition of anoxic and restricted water. Increased waterbody salinity tends to cause a decrease in biological species, but it can result in a massive bloom of specific biological species (Warren, 2012), thereby increasing productivity and promoting anoxic conditions. Therefore, compared to the SWS, the DWS had a higher degree of water restriction, a lower degree of material exchange with the outside world, and a weaker subsequent material supplement. The role of the reduced waterbody in OM preservation cannot be neglected (Gao et al., 2016). However, the water mass in the study area, particularly at the base of the QZS shales, was under highly anoxic conditions. Primary productivity is the most important influential parameter under favorable overall preservation conditions (Fig. 16). The above analysis shows that there are differences in OM enrichment under different shelf environments and that the DWS was more favorable for the formation of organic-rich sediments than SWS.

6. Conclusions

Using a combination of mineralogy and organic and elemental geochemistry, the characteristics of the QZS shales in a typical DWS–SWS transition region were analyzed, and the main controlling factors for differential OM enrichment were revealed. The main findings and conclusions of this study are as follows:

(1) During the large-scale transgression in the Early Cambrian stage and under the influence of the initial geomorphic phenomena, the DWS bore a greater amount of organic-rich sediments than the SWS.

(2) Under the overall well-preserved anoxic conditions, primary productivity was the most important factor for OM enrichment in the QZS shales.

(3) Owing to the larger sedimentary accommodation space and the promotion of hydrothermal upwelling, the sediments in the DWS had high primary productivity, which was conducive to the enrichment of high-quality organic-rich shales.

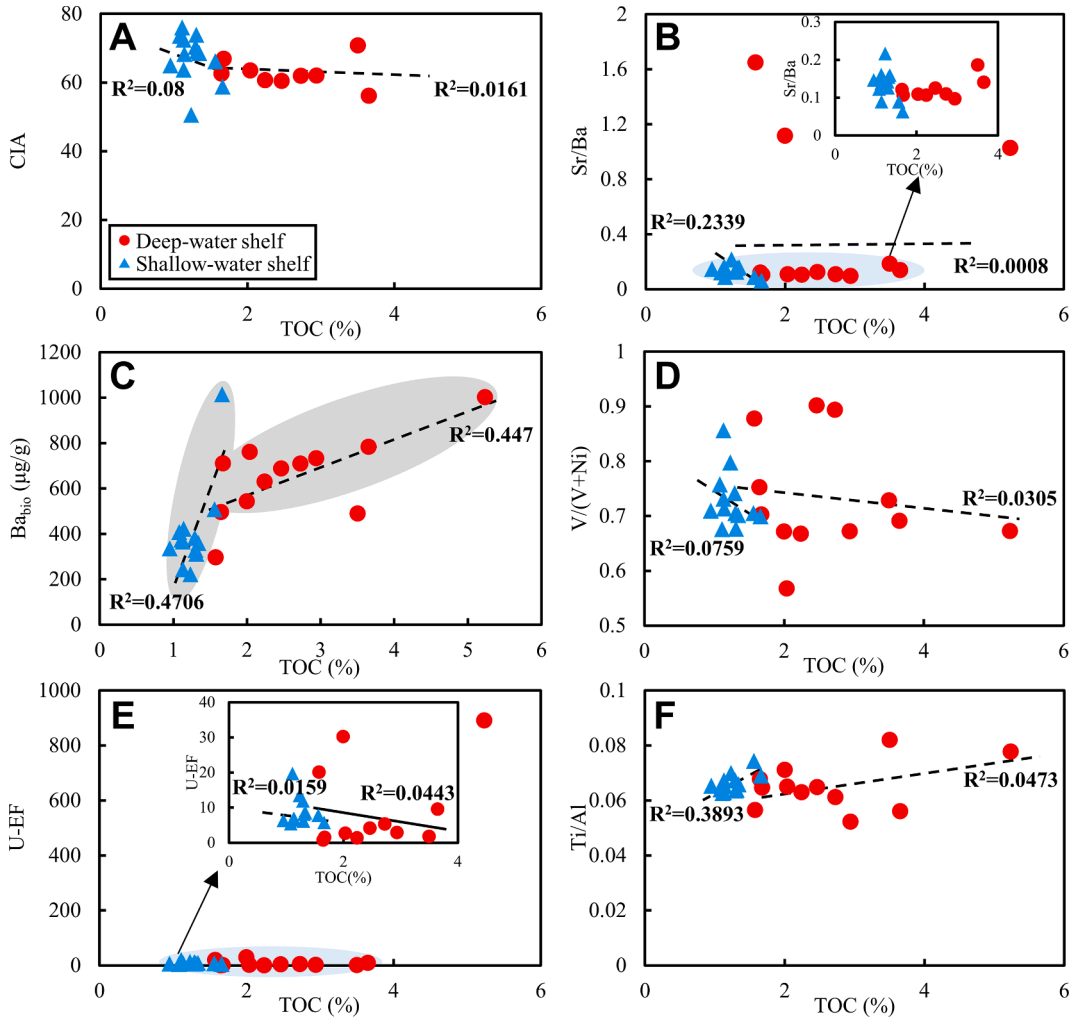

Fig. 15. Correlation diagrams between the TOC content and paleoclimate (CIA) (A), salinity (Sr/Cu) (B), primary productivity (Ba_{bio}) (C), redox conditions ((V/(V + Ni), U-EF) (D–E), and terrigenous flux (Ti/Al) (F) of shales in the Cambrian Qiongzhusi Formation of the deep-water shelf and shallow-water shelf, central Sichuan Basin.

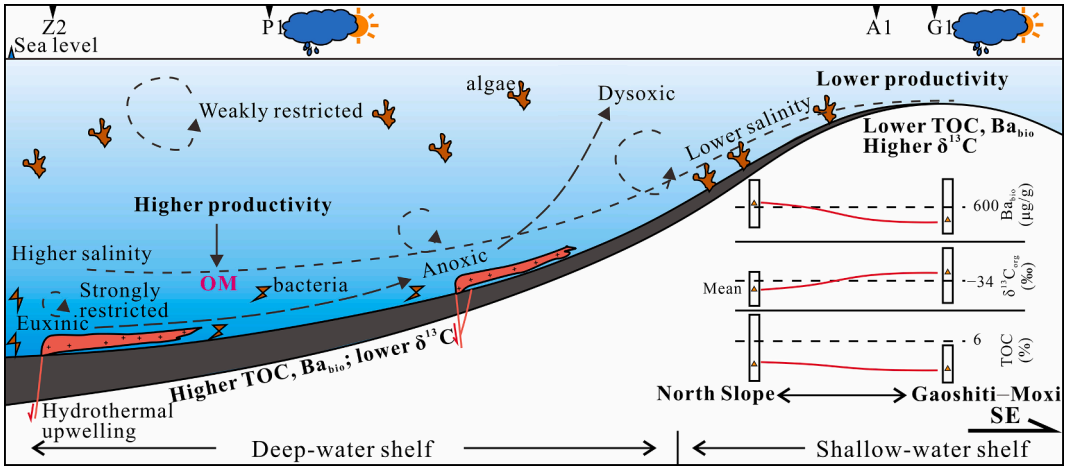

Fig. 16. Organic matter enrichment process of shales in the Cambrian Qiongzhusi Formation under different shelf conditions, central Sichuan Basin (deep-water shelf and shallow-water shelf).

CRediT authorship contribution statement

Qiang Li: Investigation, Software, Methodology, Validation, Visualization, Writing – original draft. **Guangdi Liu:** Funding acquisition, Supervision, Writing – review & editing. **Zezhang Song:** Supervision, Writing – review & editing. **Benjian Zhang:** Supervision,

Resources. **Mingliang Sun:** Supervision, Writing – review & editing. **Xingwang Tian:** Resources. **Dailin Yang:** Resources. **Yunlong Wang:** Resources. **Lianqiang Zhu:** Investigation. **Yushun Cao:** Investigation.

Declaration of Competing Interest

The authors declare that they have no known competing financial interests or personal relationships that could have appeared to influence the work reported in this paper.

Data availability

Data will be made available on request.

Acknowledgements

This research was financially supported by the National Key R&D Program of China (Grant No. 2017YFC0603106). The authors sincerely thank the Research Institute of Exploration and Development, PetroChina Southwest Oil & Gas Field Company for providing the samples and data.

Appendix A. Supplementary data

Supplementary data to this article can be found online at https://doi.org/10.1016/j.jseaes.2022.105417.

References

Adegoke, A.K., Abdullah, W.H., Hakimi, M.H., Yandoka, B.M.S., 2014. Geochemical characterisation of Fika Formation in the Chad (Bornu) Basin, northeastern Nigeria: Implications for depositional environment and tectonic setting. Appl. Geochem. 43, 1–12. https://doi.org/10.1016/j.apgeochem.2014.01.008.

Algeo, T.J., Liu, J., 2020. A re–assessment of elemental proxies for paleoredox analysis. Chem. Geol. 540, 119549. https://doi.org/10.1016/j.chemgeo.2020.119549.

Algeo, T.J., Lyons, T.W., 2006. Mo–total organic carbon covariation in modern anoxic marine environments: Implications for analysis of paleoredox and paleohydrographic conditions (PA 1016). Paleoceanography 21 (1), 23PP. https://doi.org/10.1029/2004PA001112.

Algeo, T.J., Tribovillard, N., 2009. Environmental analysis of paleoceanographic systems based on molybdenum–uranium covariation. Chem. Geol. 268 (3-4), 211–225. https://doi.org/10.1016/j.chemgeo.2009.09.001.

Allmen, K.V., Böttcher, M.E., Samankassou, E., Nägler, T.F., 2010. Barium isotope fractionation in the global barium cycle: First evidence from barium minerals and precipitation experiments. Chem. Geol. 277 (1–2), 70–77. https://doi.org/10.1016/j.chemgeo.2010.07.011.

Awan, R.S., Liu, C.L., Gong, H.W., Dun, C., Tong, C., Chamssidini, L.G., 2020. Paleo–sedimentary environment in relation to enrichment of organic matter of Early Cambrian black rocks of Niutitang Formation from Xiangxi area China. Mar. Petrol. Geol. 112, 104057. https://doi.org/10.1016/j.marpetgeo.2019.104057.

Bąk, K., 2007. Organic–rich and manganese sedimentation during the Cenomanian-Turonian boundary event in the Outer Carpathian basins; a new record from the Skole Nappe, Poland. Palaeogeogr., Palaeoclimatol., Palaeoecol. 256 (1-2), 21–46. https://doi.org/10.1016/j.palaeo.2007.09.001.

Beckmann, B., Flögel, S., Hofmann, P., Schulz, M., Wagner, T., 2005. Orbital forcing of cretaceous river discharge in tropical Africa and ocean response. Nature 437 (7056), 241–244. https://doi.org/10.1038/nature03976.

Bertrand, P., Shimmield, G., Martinez, P., Grousset, F., Jorissen, F., Paterne, M., Pujol, C., Bouloubassi, I., Menard, P.B., Peypouquet, J.-P., Beaufort, L., Sicre, M.-A., Lallier-Verges, E., Foster, J.M., Ternois, Y., 1996. The glacial ocean productivity hypothesis; the importance of regional temporal and spatial studies. Mar. Geol. 130 (1-2), 1–9. https://doi.org/10.1016/0025-3227(95)00166-2.

Calvert, S.E., Pedersen, T.F., 2007. Chapter Fourteen Elemental proxies for palaeoclimatic and palaeoceanographic variability in marine sediments: Interpretation and Application. Dev. Mar. Geol. 567–644 https://doi.org/10.1016/S1572-5480(07)01019-6.

Canfield, D.E., 1989. Reactive iron in marine sediments. Geochimica et Cosmochimica Acta 53 (3), 619–632. https://doi.org/10.1016/0016-7037(89)90005-7.

Canfield, D.E., 1994. Factors influencing organic carbon preservation in marine sediments. Chem. Geol. 114 (3-4), 315–329. https://doi.org/10.1016/0009-2541(94)90061-2.

Chen, G., Gang, W.Z., Chang, X.C., Wang, N., Zhang, P.F., Cao, Q.Y., Xu, J.B., 2020. Paleoproductivity of the Chang 7 unit in the Ordos Basin (North China) and its controlling factors. Palaeogeogr., Palaeoclimatol., Palaeoecol. 551, 109741. https://doi.org/10.1016/j.palaeo.2020.109741.

Condon, D., Zhu, M.Y., Bowring, S., Wang, W., Yang, A.H., Jin, Y.G., 2005. U-Pb ages from the neoproterozoic Doushantuo Formation, China. Science 308 (5718), 95–98.

Demaison, G.J., Moore, G.T., 1980. Anoxic environments and oil source bed genesis. Org. Geochem. 2 (1), 9–31. https://doi.org/10.1016/0146-6380(80)90017-0.

Dick, G.J., Anantharaman, K., Baker, B.J., Li, M., Reed, D.C., Sheik, C.S., 2013. The microbiology of deep–sea hydrothermal vent plumes: ecological and biogeographic linkages to seafloor and water column habitats. Front. Microbiol. 4, 1–16. https://doi.org/10.3389/fmicb.2013.00124.

Dugdale, R.C., 1972. Chemical oceanography and primary productivity in upwelling regions. Geoforum 3 (3), 47–61. https://doi.org/10.1016/0016-7185(72)90085-1.

Dunne, J.P., Armstrong, R.A., Gnanadesikan, A., Sarmiento, J.L., 2005. Empirical and mechanistic models for the particle export ratio. Glob. Biogeochem. Cycles 19 (4), GB4026. https://doi.org/10.1029/2004GB002390.

Dymond, J., Suess, E., Lyle, M., 1992. Barium in Deep-Sea Sediment: A Geochemical proxy for paleoproductivity. Paleoceanography 7 (2), 163–181. https://doi.org/10.1029/92PA00181.

Espitalie, J., LaPorte, J.L., Madec, M., Marquis, F., LePlat, P., Paulet, J., Boutefeu, A., 1977. Rapid method for source rocks characterization and for determination of petroleum potential and degree of evolution. Oil Gas Sci. Technol. 32, 23–42. https://doi.org/10.2516/ogst:1977002.

Fan, H.J., Deng, H.C., Fu, M.Y., Liu, S.B., Yu, H.Z., Li, Y.L., 2021. Sedimentary Characteristics of the Lower Cambrian Qiongzhusi Formation in the Sichuan Basin and Its Response to Construction. Acta Sedimentol. Sinica 39, 1004–1019 (in Chinese).

Fang, X.Y., Wu, L.L., Geng, A.S., Deng, Q., 2019. Formation and evolution of the Ediacaran to Lower Cambrian black shales in the Yangtze Platform, South China. Palaeogeogr., Palaeoclimatol., Palaeoecol. 527, 87–102. https://doi.org/10.1016/j.palaeo.2019.04.025.

Gao, P., Liu, G.D., Jia, C.Z., Young, A., Wang, Z.C., Wang, T.S., Zhang, P.W., Wang, D.P., 2016. Redox variations and organic matter accumulation on the Yangtze carbonate platform during Late Ediacaran-Early Cambrian: Constraints from petrology and geochemistry. Palaeogeogr., Palaeoclimatol., Palaeoecol. 450, 91–110. https://doi.org/10.1016/j.palaeo.2016.02.058.

Gao, P., Liu, G.D., Wang, Z.C., Jia, C.Z., Wang, T.S., Zhang, P.W., 2017. Rare earth elements (REEs) geochemistry of Sinian-Cambrian reservoir solid bitumens in Sichuan Basin, SW China: potential application to petroleum exploration. Geol. J. 52 (2), 298–316. https://doi.org/10.1002/gj.2757.

Gao, P., Li, S.J., Lash, G.G., Yan, D.T., Zhou, Q., Xiao, X.M., 2021. Stratigraphic framework, redox history, and organic matter accumulation of an Early Cambrian intraplatfrom basin on the Yangtze Platform, South China. Mar. Petrol. Geol. 130, 105095. https://doi.org/10.1016/j.marpetgeo.2021.105095.

Gao, P., 2016. Origin and source of Sinian bitumen in the Central Sichuan Basin. China University of Petroleum (Beijing). Doctor's thesis.

Godderis, Y., Veizer, J., 2000. Tectonic control of chemical and isotopic composition of ancient oceans; the impact of continental growth. Am. J. Sci. 300, 434–461. https://doi.org/10.2475/ajs.300.5.434.

Guo, Q.J., Strauss, H., Liu, C.Q., Goldberg, T., Zhu, M.Y., Pi, D.H., Heubeck, C., Vernhet, E., Yang, X.L., Fu, P.Q., 2007. Carbon isotopic evolution of the terminal Neoproterozoic and early Cambrian: Evidence from the Yangtze Platform, South China. Palaeogeogr., Palaeoclimatol., Palaeoecol. 254 (1–2), 140–157. https://doi.org/10.1016/j.palaeo.2007.03.014.

Hakimi, M.H., Abdullah, W.H., Makeen, Y.M., Saeed, S.A., Hakame, H.A., Moliki, T.A., Sharabi, K.Q.A., Hatem, B.A., 2017. Geochemical characterization of the Jurassic Amran deposits from Sharab area (SW Yemen): Origin of organic matter, paleoenvironmental and paleoclimate conditions during deposition. J. African Earth Sci. 129, 579–595. https://doi.org/10.1016/j.jafrearsci.2017.01.009.

Haq, B.U., Schutter, S.R., 2008. A Chronology of Paleozoic Sea-Level Changes. Science 322 (5898), 64–68.

Hatch, J.R., Leventhal, J.S., 1992. Relationship between inferred redox potential of the depositional environment and geochemistry of the Upper Pennsylvanian (Missourian) Stark Shale Member of the Dennis Limestone, Wabaunsee County, Kansas, U.S.A. Chem. Geol. 99 (1-3), 65–82. https://doi.org/10.1016/0009-2541(92)90031-Y.

Hayashi, K.-I., Fujisawa, H., Holland, H.D., Ohmoto, H., 1997. Geochemistry of ~ 1.9 Ga sedimentary rocks from northeastern Labrador, Canada. Geochimica et Cosmochimica Acta 61 (19), 4115–4137. https://doi.org/10.1016/S0016-7037(97)00214-7.

Helz, G.R., Miller, C.V., Charnock, J.M., Mosselmans, J.F.W., Pattrick, R.A.D., Garner, C. D., Vaughan, D.J., 1996. Mechanism of molybdenum removal from the sea and its concentration in black shales: EXAFS evidence. Geochimica et Cosmochimica Acta 60 (19), 3631–3642. https://doi.org/10.1016/0016-7037(96)00195-0.

Henrichs, S.M., Reeburgh, W.S., 1987. Anaerobic mineralization of marine sediment organic matter; rates and the role of anaerobic processes in the oceanic carbon economy. Geomicrobiol. J. 5 (3-4), 191–237. https://doi.org/10.1080/01490458709385971.

Hieronymus, B., Kotschoubey, B., Boulègue, J., 2001. Gallium behaviour in some contrasting lateritic profiles from Cameroon and Brazil. J. Geochem. Explor. 72 (2), 147–163. https://doi.org/10.1016/S0375-6742(01)00160-1.

Hoffman, P.F., Kaufman, A.J., Halverson, G.P., Schrag, D.P., 1998. A Neoproterozoic Snowball Earth. Science 281 (5381), 1342–1346.

Hofmann, P., Ricken, W., Schwark, L., Leythaeuser., 2000. Carbon–sulfur–iron relationships and $\delta^{13}C$ of organic matter for late Albian sedimentary rocks from the North Atlantic Ocean: paleoceanographic implications. Palaeogeogr., Palaeoclimatol., Palaeoecol. 163, 97–113. Doi: 10.1016/S0031-0182(00)00147-4.

Hossain, H.M.Z., Sampei, Y., Roser, B.P., 2009. Characterization of organic matter and depositional environment of Tertiary mudstones from the Sylhet Basin, Bangladesh. Org. Geochem. 40 (7), 743–754. https://doi.org/10.1016/j.orggeochem.2009.04.009.

Huang, J.Z., 1988. Classification basis for stable carbon isotope of kerogen. Geol. Geochem. 3, 66–68 (in Chinese).
Huang, W.W., Meinschein, W.G., 1979. Sterols as ecological indicators. Geochimica et Cosmochimica Acta 43 (5), 739–745. https://doi.org/10.1016/0016-7037(79)90257-6.
Ibach, L.E.J., 1982. Relationship between sedimentation rate and total organic carbon content in ancient marine sediments. AAPG Bull. 66, 170–188. https://doi.org/10.1306/03B59A5D-16D1-11D7-8645000102C1865D.
Jacobsen, S.B., Kaufman, A.J., 1999. The Sr, C and O isotopic evolution of Neoproterozoic seawater. Chem. Geol. 161 (1-3), 37–57. https://doi.org/10.1016/S0009-2541(99)00080-7.
Jiang, G.Q., Kaufman, A.J., Christie-Blick, N., Zhang, S.H., Wu, H.C., 2007. Carbon isotope variability across the Ediacaran Yangtze platform in South China: Implications for a large surface–to–deep ocean $\delta^{13}C$ gradient. Earth Planet. Sci. Lett. 261 (1–2), 303–320. https://doi.org/10.1016/j.epsl.2007.07.009.
Jones, B.H., 1978. A spatial analysis of the autotrophic response to abiotic forcing in three upwelling ecosystems: Oregon, northwest Africa, and Peru. Coastal Upwelling Ecosystems Analysis Technical. Report 37, 262 pp.
Jones, B., Manning, D.A.C., 1994. Comparison of geochemical indices used for the interpretation of palaeoredox conditions in ancient mudstones. Chem. Geol. 111 (1-4), 111–129. https://doi.org/10.1016/0009-2541(94)90085-X.
Kimura, H., Watanabe, Y., 2001. Oceanic anoxia at the Precambrian-Cambrian boundary. Geology 29, 995–998. https://doi.org/10.1130/0091-7613(2001)029.
Knoll, A.H., Hayes, J.M., Kaufman, A.J., Swett, K., Lambert, I.B., 1986. Secular variation in carbon isotope ratios from Upper Proterozoic successions of Svalbard and East Greenland. Nature 321 (6073), 832–838. https://doi.org/10.1038/321832a0.
Korzhinsky, M.A., Tkachenko, S.I., Shmulovich, K.I., Taran, Y.A., Steinberg, G.S., 1994. Discovery of a purerhenium mineral at Kudriavy volcano. Nature 369 (6475), 51–52. https://doi.org/10.1038/369051a0.
Krabbenhöft, A., Eisenhauer, A., Böhm, F., Vollstaedt, H., Fietzke, J., Liebetrau, V., Augustin, N., Peucker-Ehrenbrink, B., Müller, M.N., Horn, C., Hansen, B.T., Nolte, N., Wallmann, K., 2010. Constraining the marine strontium budget with natural strontium isotope fractionations ($^{87}Sr/^{86}Sr^*$, $\delta^{88/86}Sr$) of carbonates, hydrothermal solutions and river waters. Geochimica et Cosmochimica Acta 74 (14), 4097–4109. https://doi.org/10.1016/j.gca.2010.04.009.
Kulinski, K., Schneider, B., Szymczycha, B., Stokowski, M., 2017. Structure and functioning of the acid–base system in the Baltic Sea. Earth Syst. Dyn. 8, 1107–1120. https://doi.org/10.5194/esd-8-1107-2017.
Lash, G.G., Blood, D.R., 2014. Organic matter accumulation, redox, and diagenetic history of the Marcellus Formation, southwestern Pennsylvania, Appalachian Basin. Mar. Petrol. Geol. 57, 244–263. https://doi.org/10.1016/j.marpetgeo.2014.06.001.
Lewan, M.D., 1984. Factors controlling the proportionality of vanadium to nickel in crude oils. Geochimica et Cosmochimica Acta 48 (11), 2231–2238. https://doi.org/10.1016/0016-7037(84)90219-9.
Lewan, M.D., 1986. Stable carbon isotopes of amorphous kerogens from Phanerozoic sedimentary rocks. Geochimica et Cosmochimica Acta 50 (8), 1583–1591. https://doi.org/10.1016/0016-7037(86)90121-3.
Leythaeuser, D., 1973. Effects of weathering on organic matter in shales. Geochimica et Cosmochimica Acta 37 (1), 113–120. https://doi.org/10.1016/0016-7037(73)90249-4.
Li, Y.L., Fu, M.Y., Deng, H.C., Liu, S.B., Xu, W., Wu, D., 2022. The enrichment model of organic matter in the coastal detention environment: Case study of the Qiongzhusi Formation in the Gecun section of Ebian in southwestern Sichuan Basin. Nat. Gas Geosci. 33, 588–604 (in Chinese).
Li, C.R., Pang, X.Q., Ma, X.H., Wang, E.Z., Hu, T., Wu, Z.Y., 2021. Hydrocarbon generation and expulsion characteristics of the Lower Cambrian Qiongzhusi shale in the Sichuan Basin, Central China: Implications for conventional and unconventional natural gas resource potential. J. Petrol. Sci. Eng. 204, 108610. https://doi.org/10.1016/j.petrol.2021.108610.
Longhurst, A., Sathyendranath, S., Platt, T., Caverhill, C., 1995. An estimate of global primary production in the ocean from satellite radiometer data. J. Plankton Res. 17 (6), 1245–1271. https://doi.org/10.1093/plankt/17.6.1245.
Ma, D.B., Wang, Z.C., Duan, S.F., Gao, J.R., Jiang, Q.C., Jiang, H., Zeng, F.Y., Lu, W.H., 2018. Strike–slip faults and their significance for hydrocarbon accumulation in Gaoshiti-Moxi area, Sichuan Basin, SW China. Petrol. Explor. Dev. 45 (5), 851–861. https://doi.org/10.1016/S1876-3804(18)30088-0.
Ma, K., Zhang, X.H., Peng, H.L., Sun, Y.T., Yang, D.L., Zhong, J.Y., Wang, Y.L., Tian, X.W., 2020. Tectonic evolution of Moxi north slope in Sichuan Basin and its effect on forming Sinian oil and gas reservoirs. Nat. Gas Explor. Dev. 43, 8–15 (in Chinese).
Marchig, V., Gundlach, H., Möller, P., Schley, F., 1982. Some geochemical indicators for discrimination between diagenetic and hydrothermal metalliferous sediments. Mar. Geol. 50 (3), 241–256. https://doi.org/10.1016/0025-3227(82)90141-4.
McFadden, K.A., Huang, J., Chu, X.L., Jiang, G.Q., Kaufman, A.J., Zhou, C.M., Yuan, X.L., Xiao, S.H., 2008. Pulsed oxidation and biological evolution in the Ediacaran Doushantuo Formation. Proc. Natl. Acad. Sci. 105 (9), 3197–3202. https://doi.org/10.1073/pnas.0708336105.
McKibben, M.A., Williams, A.E., 1990. Solubility and transport of platinumgroup elements and Au in saline hydrothermal fluids. Constraints from the geothermal brine data. Econ. Geol. 85, 1926–1934. https://doi.org/10.2113/gsecongeo.85.8.1926.
Moradi, A.V., San, A., Akkaya, P., 2016. Geochemistry of the Miocene oil shale (Hançili Formation) in the Çankırı-Çorum Basin, Central Turkey: Implications for Paleoclimate conditions, source–area weathering, provenance and tectonic setting. Sediment. Geol. 341, 289–303. https://doi.org/10.1016/j.sedgeo.2016.05.002.
Müller, P.J., Suess, E., 1979. Productivity, sedimentation rate, and sedimentary organic matter in the oceans–I. Organic carbon preservation. Deep Sea Res. Part I. Oceanogr. Res. Pap. 26 (12), 1347–1362. https://doi.org/10.1016/0198-0149(79)90003-7.
Murphy, A.E., Sageman, B.B., Hollander, D.J., Lyons, T.W., Brett, C.E., 2000. Black shale deposition and faunal overturn in the Devonian Appalachian Basin; clastic starvation, seasonal water–column mixing, and efficient biolimiting nutrient recycling. Paleoceanography 15 (3), 280–291. https://doi.org/10.1029/1999PA000445.
Nesbitt, H.W., Young, G.M., 1982. Early Proterozoic climates and plate motions inferred from major element chemistry of lutites. Nature 299 (5885), 715–717. https://doi.org/10.1038/299715a0.
Pang, Q., Zhang, X.H., Chen, C., Gao, Z.L., Shan, S, J., Chen, Y.G., You, J., Hu, C.W., Hu, G., 2022. Extraordinarily high organic matter enrichment during the late Guadalupian in northwestern Sichuan basin, China. J. Petrol. Sci. Eng. 210, 110058. Doi: 10.1016/j.petrol.2021.110058.
Pašava, J., Ackerman, L., Žák, J., Veselovský, F., Creaser, R.A., Svojtka, M., Luais, B., Pour, O., Šebek, O., Trubač, J., Vosáhlová, E., Cividini, D., 2021. Elemental and isotopic compositions of trench–slope black shales, Bohemian Massif, with implications for oceanic and atmospheric oxygenation in early Cambrian. Palaeogeogr., Palaeoclimatol., Palaeoecol. 564, 110195. https://doi.org/10.1016/j.palaeo.2020.110195.
Pedersen, T.F., Calvert, S.E., 1990. Anoxia vs. productivity: what controls the formation of organic–carbon–rich sediments and sedimentary rocks? AAPG Bull. 74, 454–466. https://doi.org/10.1306/0C9B232B-1710-11D7-8645000102C1865D.
Peter, J.M., Goodfellow, W.D., 1996. Mineralogy, bulk and rare earth element geochemistry of massive sulphide–associated hydrothermal sediments of the Brunswick Horizon, Bathurst Mining Camp, New Brunswick. Can. J. Earth Sci. 33 (2), 252–283. https://doi.org/10.1139/e96-021.
Peters, K.E., 1986. Guidelines for evaluating petroleum source rock using programmed pyrolysis. AAPG Bull. 70, 318–329. https://doi.org/10.1306/94885688-1704-11D7-8645000102C1865D.
Qiu, N.S., Liu, W., Fu, X.D., Li, W.Z., Xu, Q.C., Zhu, C.Q., 2021. Maturity evolution of Lower Cambrian Qiongzhusi Formation shale of the Sichuan Basin. Mar. Petrol. Geol. 128, 105061. https://doi.org/10.1016/j.marpetgeo.2021.105061.
Remírez, M.N., Algeo, T.J., 2020. Paleosalinity determination in ancient epicontinental seas: A case study of the T-OAE in the Cleveland Basin (UK). Earth-Sci. Rev. 201, 103072 https://doi.org/10.1016/j.earscirev.2020.103291.
Rimmer, S.M., 2004. Geochemical paleoredox indicators in Devonian-Mississippian black shales, Central Appalachian Basin (USA). Chem. Geol. 206 (3-4), 373–391. https://doi.org/10.1016/j.chemgeo.2003.12.029.
Rimmer, S.M., Thompson, J.A., Goodnight, S.A., Robl, T.L., 2004. Multiple controls on the preservation of organic matter in Devonian-Mississippian marine black shales: geochemical and petrographic evidence. Palaeogeogr., Palaeoclimatol., Palaeoecol. 215 (1-2), 125–154. https://doi.org/10.1016/j.palaeo.2004.09.001.
Roy, D.K., Roser, B.P., 2013. Climatic control on the composition of Carboniferous-Permian Gondwana sediments, Khalaspir basin, Bangladesh. Gondwana Res. 23 (3), 1163–1171. https://doi.org/10.1016/j.gr.2012.07.006.
Rutsch, H.J., Mangini, A., Bonani, G., Hannen, B.D., Kubik, P.W., Suter, M., Segl, M., 1995. ^{10}Be and Ba concentrations in West African sediments trace productivity in the past. Earth Planet. Sci. Lett. 133 (1–2), 129–143. https://doi.org/10.1016/0012-821X(95)00069-O.
Ryther, J.H., Dunstan, W.M., 1971. Nitrogen, phosphorus, and eutrophication in the coastal marine environment. Science 171 (3975), 1008–1013.
Sageman, B.B., Murphy, A.E., Werne, J.P., Ver Straeten, C.A., Hollander, D.J., Lyons, T.W., 2003. A tale of shales: the relative roles of production, decomposition, and dilution in the accumulation of organic–rich strata, Middle-Upper Devonian, Appalachian Basin. Chem. Geol. 195 (1-4), 229–273. https://doi.org/10.1016/S0009-2541(02)00397-2.
Schoepfer, S.D., Shen, J., Wei, H.Y., Tyson, R.V., Ingall, E., Algeo, T.J., 2015. Total organic carbon, organic phosphorus, and biogenic barium fluxes as proxies for paleomarine productivity. Earth-Sci. Rev. 149, 23–52. https://doi.org/10.1016/j.earscirev.2014.08.017.
Shen, J., Lei, Y., Algeo, T.J., Feng, Q.L., Servais, T., Yu, J.X., Zhou, L., 2013. Volcanic effects on microplankton during the Permian-Triassic transition (Shangsi and Xinmin, South China). Palaios 28 (8), 552–567. https://doi.org/10.2110/palo.2013.p13-014r.
Shen, J., Zhou, L., Feng, Q.L., Zhang, M.H., Lei, Y., Zhang, N., Yu, J.X., Gu, S.Z., 2014. Paleo–productivity evolution across the Permian-Triassic boundary and quantitative calculation of primary productivity of black rock series from the Dalong Formation, South China. Sci. China: Earth Sci. 57 (7), 1583–1594. https://doi.org/10.1007/s11430-013-4780-5.
Shen, J., Schoepfer, S.D., Feng, Q.L., Zhou, L., Yu, J.X., Song, H.Y., Wei, H.Y., Algeo, T.J., 2015. Marine productivity changes during the end–Permian crisis and Early Triassic recovery. Earth-Sci. Rev. 149, 136–162. https://doi.org/10.1016/j.earscirev.2014.11.002.
Shi, C.H., Cao, J., Tan, X.C., Luo, B., Zeng, W., Hong, H.T., Huang, X., Wang, Y., 2018. Hydrocarbon generation capability of Sinian-Lower Cambrian shale, mudstone, and carbonate rocks in the Sichuan Basin, southwestern China: Implications for contributions to the giant Sinian Dengying natural gas accumulation. AAPG Bull. 102 (05), 817–853. https://doi.org/10.1306/0711171417417019.
Shi, C.H., Cao, J., Luo, B., Hu, W.X., Tan, X.C., Tian, X.W., 2020. Major elements trace hydrocarbon sources in over–mature petroleum systems: Insights from the Sinian Sichuan Basin, China. Precambrian Res. 343, 105726. https://doi.org/10.1016/j.precamres.2020.105726.

Shields, G., Stille, P., 2001. Diagenetic constraints on the use of cerium anomalies as palaeoseawater redox proxies: an isotopic and REE study of Cambrian phosphorites. Chem. Geol. 175, 29–48. https://doi.org/10.1016/S0009-2541(00)00362-4.

Shiller, A.M., Frilot, D.M., 1996. The geochemistry of gallium relative to aluminum in Californian streams. Geochimica et Cosmochimica Acta 60 (8), 1323–1328. https://doi.org/10.1016/0016-7037(96)00002-6.

Song, W.H., 1996. Reservoir–forming conditions of large to medium gasfields in Leshan-Longnvsi palaeohigh. Nat. Gas Ind. 16, 13–26 (in Chinese).

Song, L.S., Bhattacharya, S., Webb, Z., Fowler, A., Lee, V., 2021. Preservation of organic carbon in the Cretaceous Hue Shale on the North Slope of Alaska: Insights from pyrite morphology. Int. J. Coal Geol. 235, 103678. https://doi.org/10.1016/j.coal.2021.103678.

Suess, E., Thiede, J., 2013. Coastal Upwelling its Sediment Record: Part A: Responses of the Sedimentary Regime to Present Coastal Upwelling, vol. 10. Springer Science and Business Media.

Tan, Z.Z., Lu, S.F., Li, W.H, Zhang, Y.Y., He, T.H., Jia, W.L., Peng, P.A., 2019. Climate-Driven Variations in the Depositional Environment and Organic Matter Accumulation of Lacustrine Mudstones: Evidence from organic and inorganic geochemistry in the Biyang Depression, Nanxiang Basin, China. Energy Fuels 33 (8), 6946–6960. https://doi.org/10.1021/acs.energyfuels.9b00595.

Tan, Z.Z., Jia, W.L., Li, J., Yin, L., Wang, S.S., Wu, J.X., Song, J.Z., Peng, P.A., 2021. Geochemistry and molybdenum isotopes of the basal Datangpo Formation: Implications for ocean–redox conditions and organic matter accumulation during the Cryogenian interglaciation. Palaeogeogr., Palaeoclimatol., Palaeoecol. 563, 110169. https://doi.org/10.1016/j.palaeo.2020.110169.

Taylor, S.R., McLennan, S.M., 1985. The Continental Crust: Its Composition and Evolution. Blackwell Scientific Publication, Oxford, p. 312.

Tostevin, R., Shields, G.A., Tarbuck, G.M., He, T.C., Clarkson, M.O., Wood, R.A., 2016. Effective use of cerium anomalies as a redox proxy in carbonate–dominated marine settings. Chem. Geol. 438, 146–162. https://doi.org/10.1016/j.chemgeo.2016.06.027.

Tribovillard, N., Algeo, T.J., Lyons, T., Riboulleau, A., 2006. Trace metals as paleoredox and paleoproductivity proxies: An update. Chem. Geol. 232 (1-2), 12–32. https://doi.org/10.1016/j.chemgeo.2006.02.012.

Tribovillard, N., Algeo, T.J., Baudin, F., Riboulleau, A., 2012. Analysis of marine environmental conditions based on molybdenum–uranium covariation–Applications to Mesozoic paleoceanography. Chem. Geol. 324–325, 46–58. https://doi.org/10.1016/j.chemgeo.2011.09.009.

Tyson, R.V., 2001. Sedimentation rate, dilution, preservation and total organic carbon: some results of a modelling study. Org. Geochem. 32 (2), 333–339. https://doi.org/10.1016/S0146-6380(00)00161-3.

Veizer, J., Buhl, D., Diener, A., Ebneth, S., Podlaha, O.G., Bruckschen, P., Jasper, T., Korte, C., Schaaf, M., Ala, D., Azmy, K., 1997. Strontium isotope stratigraphy: potential resolution and event correlation. Palaeogeogr., Palaeoclimatol., Palaeoecol. 132 (1-4), 65–77. https://doi.org/10.1016/S0031-0182(97)00054-0.

Walter, M.R., Veevers, J.J., Calver, C.R., Gorjan, P., Hill, A.C., 2000. Dating the 840–544 Ma Neoproterozoic interval by isotopes of strontium, carbon, sulfur in seawater, and some interpretative models. Precambrian Res. 100, 371–433. https://doi.org/10.1016/S0301-9268(99)00082-0.

Wang, N., Li, M.J., Hong, H.T., Song, D.F., Tian, X.W., Liu, P., Fang, R.H., Chen, G., Wang, M.L., 2019. Biological sources of sedimentary organic matter in Neoproterozoic-Lower Cambrian shales in the Sichuan Basin (SW China): Evidence from biomarkers and microfossils. Palaeogeogr., Palaeoclimatol., Palaeoecol. 516, 342–353. https://doi.org/10.1016/j.palaeo.2018.12.012.

Wang, N., Li, M.J., Tian, X.W., Hong, H.T., Wen, L., Wang, W.Z., 2020. Climate–ocean control on the depositional watermass conditions and organic matter enrichment in lower Cambrian black shale in the upper Yangtze Platform. Mar. Petrol. Geol. 120, 104570. https://doi.org/10.1016/j.marpetgeo.2020.104570.

Wang, N., Wen, L., Li, M.J., Dai, X., Xu, Y.H., Ming, Y., Yang, S., 2021. The origin of abnormally ^{13}C–depleted organic carbon isotope signatures in the early Cambrian Yangtze Platform. Mar. Petrol. Geol. 128, 105051. https://doi.org/10.1016/j.marpetgeo.2021.105051.

Wang, S.F., Zou, C.N., Dong, D.Z., Wang, Y.M., Li, X.J., Huang, J.L., Guan, Q.Z., 2015. Multiple controls on the paleoenvironment of the Early Cambrian marine black shales in the Sichuan Basin, SW China: Geochemical and organic carbon isotopic evidence. Mar. Petrol. Geol. 66, 660–672. https://doi.org/10.1016/j.marpetgeo.2015.07.009.

Warren, J.K., 2012. Evaporitic source rocks: mesohaline responses to cycles of “famine or feast” in layered brines. Quaternary Carbonate and Evaporite Sedimentary Facies and Their Ancient Analogues 43, 315–392. https://doi.org/10.1002/9781444392326.ch16.

Wei, W., Algeo, T.J., 2020. Elemental proxies for paleosalinity analysis of ancient shales and mudrocks. Geochimica et Cosmochimica Acta 287, 341–366. https://doi.org/10.1016/j.gca.2019.06.034.

Wei, G.Q., Wang, D.L., Wang, X.B., Li, J., Li, Z.S., Xie, Z.Y., Cui, H.Y., Wang, Z.H., 2014. Characteristics of noble gases in the large Gaoshiti-Moxi gas field in Sichuan Basin, SW China. Petrol. Explor. Dev. 41 (5), 585–590. https://doi.org/10.1016/S1876-3804(14)60069-0.

Wei, G.Q, Xie, Z.Y, Song, J.R., Yang, W., Wang, Z.H., Li, J., Wang, D.L., Li, Z.S., Xie, W.R., 2015. Features and origin of natural gas in the Sinian-Cambrian of central Sichuan paleo–uplift, Sichuan Basin, SW China. Petrol. Explor. Dev. 42 (6), 768–777. https://doi.org/10.1016/S1876-3804(15)30073-2.

Wei, G.Q., Wang, Z.C., Li, J., Yang, W., Xie, Z.Y., 2017. Characteristics of source rocks, resource potential and exploration direction of Sinian-Cambrian in Sichuan Basin, China. J. Nat. Gas Geosci. 2 (5–6), 289–302. https://doi.org/10.1016/j.jnggs.2018.02.002.

Wignall, P.B., Twitchett, R.J., 1996. Oceanic Anoxia and the End Permian Mass Extinction. Science 272 (5265), 1155–1158.

Williams, T.S., Bhattacharya, S., Song, L.S., Agrawal, V., Sharma, S., 2022. Petrophysical analysis and mudstone lithofacies classification of the HRZ shale, North Slope, Alaska. J. Petrol. Sci. Eng. 208, 109454. https://doi.org/10.1016/j.petrol.2021.109454.

Wu, Y.W., Tian, H., Gong, D.J., Li, T.F., Zhou, Q., 2020. Paleo–environmental variation and its control on organic matter enrichment of black shales from shallow shelf to slope regions on the Upper Yangtze Platform during Cambrian Stage 3. Palaeogeogr., Palaeoclimatol., Palaeoecol. 545, 109653. https://doi.org/10.1016/j.palaeo.2020.109653.

Xiao, S.H., Bykova, N., Kovalick, A., Gill, B.C., 2017. Stable carbon isotopes of sedimentary kerogens and carbonaceous macrofossils from the Ediacaran Miaohe Member in South China: Implications for stratigraphic correlation and sources of sedimentary organic carbon. Precambrian Res. 302, 171–179. https://doi.org/10.1016/j.precamres.2017.10.006.

Xiao, D., Cao, J., Luo, B., Tan, X., Xiao, W.Y., He, Y., Li, K.Y., 2021. Neoproterozoic postglacial paleoenvironment and hydrocarbon potential: A review and new insights from the Doushantuo Formation Sichuan Basin, China. Earth-Sci. Rev. 212, 103453. https://doi.org/10.1016/j.earscirev.2020.103453.

Xu, L., Lehmann, B., M, J.W., Q, W.J., Andao, D., 2011. Re–Os age of polymetallic Ni–Mo–PGE–Au mineralization in early Cambrian black shales of South China—a reassessment. Econ. Geol. 106 (3), 511–522. https://doi.org/10.2113/econgeo.106.3.511.

Xu, C.C., Shen, P., Yang, Y.M., Zhao, L.Z., Luo, B., Wen, L., Chen, K., Ran, Q., Zhong, Y., Peng, H.L., 2020. New understandings and potential of Sinian-Lower Paleozoic natural gas exploration in the central Sichuan paleo–uplift of the Sichuan Basin. Nat. Gas Ind. 8, 105–113. https://doi.org/10.1016/j.ngib.2020.07.007.

Xu, H.L., Wei, G.Q., Jia, C.Z., Yang, W., Zhou, T.W., Xie, W.R., Li, C.X., Luo, B.W., 2012. Tectonic evolution of the Leshan-Longnvsi paleo–uplift and its control on gas accumulation in the Sinian strata, Sichuan Basin. Petrol. Explor. Dev. 39, 436–446. https://doi.org/10.1016/S1876-3804(12)60060-3.

Yan, D.T., Wang, H., Fu, Q.L., Chen, Z.H., He, J., Cao, Z., 2015a. Geochemical characteristics in the Longmaxi Formation (Early Silurian) of South China: Implications for organic matter accumulation. Mar. Petrol. Geol. 65, 290–301. https://doi.org/10.1016/j.marpetgeo.2015.04.016.

Yan, D.T., Wang, H., Fu, Q.L., Chen, Z.H., He, J., Cao, Z., 2015b. Organic matter accumulation of Late Ordovician sediments in North Guizhou Province, China: Sulfur isotope and trace element evidences. Mar. Petrol. Geol. 59, 348–358. https://doi.org/10.1016/j.marpetgeo.2014.09.017.

Yang, Y., Luo, B., Zhang, B.J., Xiao, D., Xiao, W.Y., Cao, J., 2021. Differential mechanisms of organic matter accumulation of source rocks in the Lower Cambrian Qiongzhusi Formation and implications for gas exploration fields in Sichuan Basin. Petrol. Geol. Exp. 43, 611–619 (in Chinese).

Yang, H., Yang, L.S., Zhou, M.Z., 2022. Expanded deepwater euxinia recorded in the Ediacaran-Cambrian boundary interval in South China. J. Asian Earth Sci. 230, 105192. https://doi.org/10.1016/j.jseaes.2022.105192.

Yeasmin, R., Chen, D.Z., Fu, Y., Wang, J.G., Guo, Z.H., Guo, C., 2017. Climatic–oceanic forcing on the organic accumulation across the shelf during the Early Cambrian (Age 2 through 3) in the mid–upper Yangtze Block, NE Guizhou, South China. J. Asian Earth Sci. 134, 365–386. https://doi.org/10.1016/j.jseaes.2016.08.019.

Zhang, C.Y., Guan, S.W., Wu, L., Ren, R., Wang, L.N., Wu, X.Q., 2020. Depositional environments of early Cambrian marine shale, northwestern Tarim Basin, China: Implications for organic matter accumulation. J. Petrol. Sci. Eng. 194, 107497. https://doi.org/10.1016/j.petrol.2020.107497.

Zhang, K.X., Li, X.S., Wang, Y.X., Liu, W., Yu, Y.X., Zhou, L., Feng, W.P., 2021a. Paleo–environments and organic matter enrichment in the shales of the Cambrian Niutitang and Wunitang Formations, south China: Constraints from depositional environments and geochemistry. Mar. Petrol. Geol. 134, 105329 https://doi.org/10.1016/j.marpetgeo.2021.105329.

Zhang, X.T., Shen, B., Yang, J.J., Sun, W.L., Hou, D.J., 2021b. Evolution characteristics of maturity–related sterane and terpane biomarker parameters during hydrothermal experiments in a semi–open system under geological constraint. J. Petrol. Sci. Eng. 201, 108412 https://doi.org/10.1016/j.petrol.2021.108412.

Zhang, Q., Wang, J., Yu, Q., Wang, X.F., Zhao, A.K., Lei, Z.H., 2017. Geochemical Features and Paleoenvironment of shales in Longmaxi Formation of Complicated Structure Area, Southwestern Sichuan Basin. Xinjiang Petrol. Geol. 38, 399–406 (in Chinese).

Zhang, B.L., Yao, S.P., Wignall, P.B., Hu, W.X., Ding, H., Liu, B., Ren, Y.L., 2018. Widespread coastal upwelling along the Eastern Paleo-Tethys Margin (South China) during the Middle Permian (Guadalupian): Implications for organic matter accumulation. Mar. Petrol. Geol. 97, 113–126. https://doi.org/10.1016/j.marpetgeo.2018.06.025.

Zhao, L.K., Li, W.H., He, Y., Zhou, H.F., Liu, R., Li, Y., Wang, W., Zhong, Y., Wang, Y.Y., 2020a. Sedimentation and filling laws of Maidiping-Qiongzhusi formations in Sichuan Basin and their significance of oil and gas geological exploration. Nat. Gas Explor. Dev. 43, 30–38 (in Chinese).

Zhao, L.Z., Wang, Z.C., Yang, Y., Duan, S.F., Wei, G.Q., Luo, B., Wen, L., Ma, S.Y., Feng, Q.F., Liu, J.J., Sun, X.P., Xie, W.R., 2020b. Important discovery in the second member of Dengying Formation in Well Pengtan1 and its significance, Sichuan Basin. China Petrol. Explor. 25, 1–12 (in Chinese).

Zhao, Z.Y., Zhao, J.H., Wang, H.J., Liao, J.D., Liu, C.M., 2007. Distribution characteristics and applications of trace elements in Junggar basin. Nat. Gas Explor. Dev. 30, 30–33 (in Chinese).

Zhu, L.Q., Liu, G.D., Song, Z.Z., Zhao, W.Z., Li, Q., Tian, X.W., Wang, Y.L., Yang, D.L., 2022. Reservoir solid bitumen–source rock correlation using the trace and rare earth

elements–implications for identifying the natural gas source of the Ediacaran-Lower Cambrian reservoirs, central Sichuan Basin. Mar. Petrol. Geol. 137, 105499. https://doi.org/10.1016/j.marpetgeo.2021.105499.

Zhu, G.Y., Wang, T.S., Xie, Z.Y., Xie, B.H., Liu, K.Y., 2015. Giant gas discovery in the Precambrian deeply buried reservoirs in the Sichuan Basin, China: implications for gas exploration in old cratonic basins. Precambrian Res. 262, 45–66. https://doi.org/10.1016/j.precamres.2015.02.023.

Zou, C.N., Wei, G.Q., Xu, C.C., Du, J.H., Xie, Z.Y., Wang, Z.C., Hou, L.H., Yang, C., Li, J., Yang, W., 2014. Geochemistry of the Sinian-Cambrian gas system in the Sichuan Basin, China. Org. Geochem. 74, 13–21. https://doi.org/10.1016/j.orggeochem.2014.03.004.

Zou, C.N., Zhu, R.K., Chen, Z.Q., Ogg, J.G., Wu, S.T., Dong, D.Z., Qiu, Z., Wang, Y.M., Wang, L., Lin, S.H., Cui, J.W., Su, L., Yang, Z., 2019. Organic–matter–rich shales of China. Earth-Sci. Rev. 189, 51–78. https://doi.org/10.1016/j.earscirev.2018.12.002.